

ASASSN-18am/SN 2018gk: An overluminous Type IIb supernova from a massive progenitor

Subhash Bose,^{1,2*} Subo Dong,^{3†} C. S. Kochanek,^{1,2} M. D. Stritzinger,⁴ Chris Ashall,⁵ Stefano Benetti,⁶ E. Falco,⁷ Alexei V. Filippenko,^{8,9} Andrea Pastorello,⁶ Jose L. Prieto,^{10,11} Auni Somero,¹² Tuguldur Sukhbold,^{1,2} Junbo Zhang,¹³ Katie Auchettl,^{14,15,16,17} Thomas G. Brink,⁸ J. S. Brown,¹⁸ Ping Chen,³ A. Fiore,^{6,19} Dirk Grupe,²⁰ T. W.-S. Holoien,²¹ Peter Lundqvist,²² Seppo Mattila,¹² Robert Mutel,²³ David Pooley,²⁴ R. S. Post,²⁵ Naveen Reddy,²⁶ Thomas M. Reynolds,¹² Benjamin J. Shappee,²⁷ K. Z. Stanek,^{1,2} Todd A. Thompson,^{1,2} S. Villanueva Jr.,¹ and WeiKang Zheng⁸

Affiliations are listed at the end of the paper

Accepted.....; Received

ABSTRACT

ASASSN-18am/SN 2018gk is a newly discovered member of the rare group of luminous, hydrogen-rich supernovae (SNe) with a peak absolute magnitude of $M_V \approx -20$ mag that is in between normal core-collapse SNe and superluminous SNe. These SNe show no prominent spectroscopic signatures of ejecta interacting with circumstellar material (CSM), and their powering mechanism is debated. ASASSN-18am declines extremely rapidly for a Type II SN, with a photospheric-phase decline rate of ~ 6.0 mag $(100 \text{ d})^{-1}$. Owing to the weakening of H I and the appearance of He I in its later phases, ASASSN-18am is spectroscopically a Type IIb SN with a partially stripped envelope. However, its photometric and spectroscopic evolution show significant differences from typical SNe IIb. Using a radiative diffusion model, we find that the light curve requires a high synthesised ^{56}Ni mass $M_{\text{Ni}} \sim 0.4 M_{\odot}$ and ejecta with high kinetic energy $E_{\text{kin}} = (7-10) \times 10^{51}$ erg. Introducing a magnetar central engine still requires $M_{\text{Ni}} \sim 0.3 M_{\odot}$ and $E_{\text{kin}} = 3 \times 10^{51}$ erg. The high ^{56}Ni mass is consistent with strong iron-group nebular lines in its spectra, which are also similar to several SNe Ic-BL with high ^{56}Ni yields. The earliest spectrum shows “flash ionisation” features, from which we estimate a mass-loss rate of $\dot{M} \approx 2 \times 10^{-4} M_{\odot} \text{ yr}^{-1}$. This wind density is too low to power the luminous light curve by ejecta-CSM interaction. We measure expansion velocities as high as $17,000 \text{ km s}^{-1}$ for H α , which is remarkably high compared to other SNe II. We estimate an oxygen core mass of $1.8-3.4 M_{\odot}$ using the [O I] luminosity measured from a nebular-phase spectrum, implying a progenitor with a zero-age main sequence mass of $19-26 M_{\odot}$.

Key words: supernovae: general – supernovae: individual: (ASASSN-18am/ SN 2018gk) – galaxies: individual: WISE J163554.27+400151.8

1 INTRODUCTION

Supernovae (SNe) originating from massive stars ($\gtrsim 10 M_{\odot}$) that have retained a significant amount of hydrogen at the time of explosion show strong Balmer lines in their spectra and are classified

as Type II SNe (e.g., Filippenko 1997). Several subclasses have been introduced to this hydrogen-rich class of SNe based on photometric or spectroscopic properties. Historically, the Type IIP and III subclasses (Barbon et al. 1979; Doggett & Branch 1985) were mainly motivated by light-curve shapes in the photospheric phase ($\lesssim 100$ d), where the former show a distinct “plateau” in the light-curve and the latter show a “linear” decline in magnitude. With increasing numbers of SNe discovered by systematic surveys, it be-

* e-mail: email@subhashbose.com, bose.48@osu.edu

† e-mail: dongsubo@pku.edu.cn

came increasingly clear that normal SN II light-curve shapes form a continuous distribution (e.g., [Anderson et al. 2014](#); [Faran et al. 2014](#); [Sanders et al. 2015](#)), suggesting a continuum in their ejecta properties. Hereafter, we refer to this entire class as a combined SN IIP/L class, or with the general designation SNe II, while we occasionally mention SNe IIP and IIL as two extremes of the light-curve slope distribution.

Two additional subclasses of SNe II, which are differentiated by their spectroscopic properties, are SNe IIn and IIb. The spectra of SNe IIn show relatively narrow ($< 100 \text{ km s}^{-1}$) or intermediate-width ($\sim 1000 \text{ km s}^{-1}$) emission lines, which are believed to result from strong interactions between the ejecta and circumstellar material (CSM) ([Schlegel 1990](#)). These interactions act as an additional power source and can produce light curves significantly different from those of normal SNe II. SNe IIb constitute a transition class of objects linking SNe II and Ib ([Filippenko 1988](#); [Filippenko et al. 1993](#)). The spectra of SNe IIb show prominent hydrogen lines at early times, while helium lines become visible after a few weeks. The hydrogen envelope of a SN IIb is thought to be partially stripped so that the helium core is revealed as the envelope becomes optically thin.

The primary powering mechanisms in normal SNe II are ^{56}Ni decay and internal energy deposited by the shock in the ejecta. During the post-photospheric phase, when the ejecta become optically thin, light curves of all common SN types (both core-collapse SNe and SNe Ia) are powered by energy deposition from the radioactive decay chain of $^{56}\text{Ni} \rightarrow ^{56}\text{Co} \rightarrow ^{56}\text{Fe}$, with the exception of some SNe that undergo strong ejecta-CSM interactions during late phases. The light-curve slopes during the radioactive-powered phase depend on the amount of γ -ray leakage, which is determined by the ejecta properties.

Hydrogen-rich luminous SNe (LSNe-II)

Over the last decade or so, a new subclass of SNe called superluminous supernovae (SLSNe) has emerged, based on their high peak luminosities compared to common SN types. The hydrogen-poor subclass of SLSNe (SLSNe-I; [Quimby et al. 2007, 2011](#)) have peak luminosities $M_g \lesssim -20 \text{ mag}$ ([Gal-Yam 2019](#)), which are significantly more luminous than common SNe (SNe Ia, IIP/L, and Ib/c). There is no systematic study of the luminosity distribution of SLSNe-II, but many known SLSNe-II show strong CSM interaction (SLSNe-IIn), and the average peak luminosities of SLSNe-IIn are estimated to be $\sim -21 \text{ mag}$ ([Gal-Yam 2019](#)).

In the last few years, a handful of luminous hydrogen-rich SNe have been found with no prominent signatures of CSM interaction and optical luminosities of $\sim -20 \text{ mag}$ (e.g., PTF10iam by [Arcavi et al. 2016](#), SN 2013fc by [Kangas et al. 2016](#), ASASSN-15nx by [Bose et al. 2018](#), and SN 2016gsd by [Reynolds et al. 2020](#)). Hereafter we refer to these luminous hydrogen-rich SNe as ‘‘LSNe-II’’. We stress that it is not yet clear whether LSNe-II form a distinct subclass of SNe II. [Bose et al. \(2018\)](#) showed that their volumetric rate might be comparable to that of SLSNe based on the single discovery of ASASSN-15nx, providing an intriguing yet tentative possibility that they might be part of a continuous luminosity distribution connecting normal SNe with SLSNe.

LSNe-II have numerous light-curve and spectroscopic peculiarities, and it is challenging to explain their luminosities with the commonly proposed mechanisms for core-collapse supernovae (cc-SNe). None of these SNe shows persistent narrow emission lines indicating strong ejecta-CSM interaction as seen in luminous SNe IIn. However, the lack of narrow emission lines may not be sufficient

to entirely rule out CSM interaction. In all of the LSNe-II studies to date, CSM interaction is considered as at least one of the possible powering sources, where certain CSM configurations may be able to hide the strong emission lines and leave only weak spectroscopic features to be associated with CSM interaction. [Bose et al. \(2018\)](#) also showed that the light curves of ASASSN-15nx could be entirely powered by radioactive decay but required a very large amount of ^{56}Ni ($M_{\text{Ni}} \approx 1.6 M_{\odot}$). However, this scenario may not be tenable given the lack of strong lines of iron-group elements in its spectra. Such a high ^{56}Ni mass is not compatible with the neutrino mechanism of ccSNe (see, e.g., [Sukhbold et al. 2016](#); [Ertl et al. 2020](#)), but it is possible for collapse-induced thermonuclear explosions ([Burbidge et al. 1957](#); [Hoyle & Fowler 1960](#); [Fowler & Hoyle 1964](#); [Kushnir 2015b,a](#); [Kushnir & Katz 2015](#)) or pair-instability SNe (e.g., [Barkat et al. 1967](#); [Kasen et al. 2011](#)). However, pair-instability SN models exhibit extended light curves which are incompatible with ASASSN-15nx and most other LSNe-II. For ASASSN-15nx, [Chugai \(2019\)](#) also suggested magnetar spin-down as an alternate powering mechanism based on detailed spectroscopic and light-curve modeling.

Here, we report the latest addition to this rare and underexplored group of LSNe-II, ASASSN-18am, with a peak luminosity of $M_V \approx -19.7 \text{ mag}$. We present a detailed study of this SN from its discovery to well into the nebular phase. In §2 we discuss the adopted values for the distance, explosion epoch, and line-of-sight extinction, along with the host-galaxy properties. The data obtained from various telescopes are summarised in §3. The light curve and spectra are analysed in §4 and §5, respectively. In §6, we discuss various powering mechanisms through modeling. Nebular-phase emission lines are analysed in §7, and we estimate oxygen and zero-age main sequence (ZAMS) masses of the progenitor. We summarise our findings in §8.

2 EXPLOSION EPOCH, EXTINCTION, AND HOST PROPERTIES

ASASSN-18am/SN 2018gk (J2000 coordinates $\alpha = 16^{\text{h}}35^{\text{m}}54^{\text{s}}.60$, $\delta = +40^{\circ}01'58''01$) was discovered ([Brimacombe et al. 2018](#)) in the galaxy WISE J163554.27+400151.8 (see Fig. 1 for an image of the SN and host galaxy) by the All-Sky Automated Survey for Supernovae (ASAS-SN; [Shappee et al. 2014](#); [Kochanek et al. 2017](#)). ASASSN-18am was first detected by ASAS-SN on 2018-01-12.5 (UT dates are used throughout this paper) at a g-band magnitude of 16.8. Based on the last nondetection on 2018-01-11.7 at a limit of $V = 17.6 \text{ mag}$, we choose an explosion epoch of 2018-01-12.1 (JD 2, 458, 130.6 ± 0.4).

We adopt a total line-of-sight reddening of $E(B - V) = 0.0086 \pm 0.0011 \text{ mag}$ ([Schlafly & Finkbeiner 2011](#)), which is entirely due to the Milky Way. We neglect any host-galaxy extinction owing to the absence of any Na I D absorption at the host redshift in all our spectra, indicating a very low or negligible contribution from the host galaxy. Assuming $R_V = 3.1$, this corresponds to $A_V = 0.027 \pm 0.003 \text{ mag}$.

The host WISE J163554.27+400151.8 is a late-type galaxy ([Lee et al. 2015](#)) at a redshift of 0.031010 ± 0.000005 ([SDSS Collaboration et al. 2017](#)). This gives a luminosity distance of $D_L = 140.5 \pm 2.3 \text{ Mpc}$ assuming a standard *Planck* cosmology ([Planck Collaboration et al. 2016](#)).

We used ultraviolet (UV) to mid-infrared data from *Galex*, the Sloan Digital Sky Survey (SDSS), and *WISE* to fit the spectral energy distribution (SED) with the FAST code ([Kriek et al. 2009](#)) and

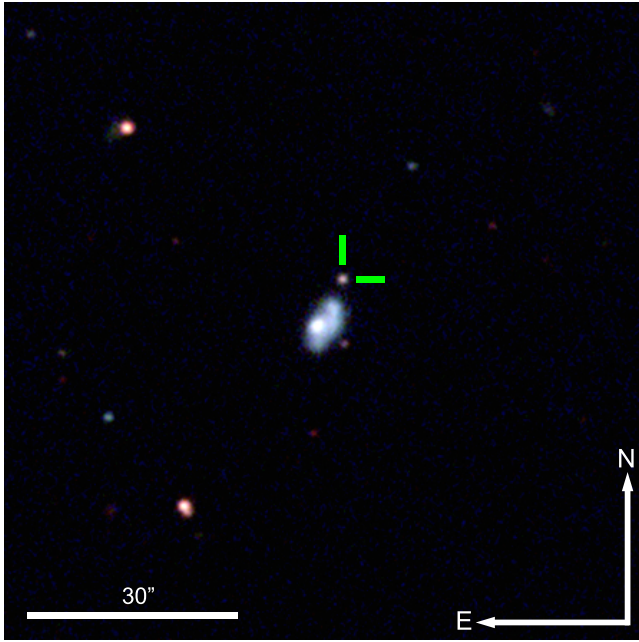


Figure 1. $1.5' \times 1.5'$ *BgrI*-band composite image from the Liverpool Telescope observed 131 days after explosion showing ASASSN-18am in the host galaxy WISE J163554.27+400151.8.

estimate the properties of the host galaxy. We derived a host stellar mass of $\log(M_*/M_\odot) = 8.98^{+0.09}_{-0.08}$ and a specific star formation rate of $\log(\text{sSFR}) = -9.83^{+0.10}_{-0.03}$. The oxygen abundance in the MPA-JHU catalog (Brinchmann et al. 2004) is $12 + \log(\text{O}/\text{H}) = 8.6$ on the Tremonti et al. (2004) scale, implying roughly solar metallicity. The host properties of ASASSN-18am are typical of ccSN hosts (see, e.g., Kelly & Kirshner 2012). This SDSS oxygen abundance is based on a spectrum centred on the host’s apparent nucleus, so the metallicity at the site of the SN is likely much lower since its projected separation of ~ 5 kpc is outside the optical disk (see Fig. 1).

3 OBSERVATIONS AND DATA

Multiband photometric and spectroscopic observations were initiated soon after the discovery and were continued for 218 days (observer frame). Optical photometric data were obtained with the ASAS-SN quadruple 14 cm “Brutus” telescope, the Las Cumbres Observatory 1.0 m telescope network (LCOGT; Brown et al. 2013), the 0.6 m telescopes at Post Observatory SRO (CA, USA) and Post Observatory Mayhill (NM, USA), the 0.5 m DEDicated MONitor of EXotransits and Transients (DEMONEXT; Villanueva et al. 2016, 2018), the 0.5 m Iowa Robotic Telescope (both at the Winer Observatory, AZ, USA), and the 2.0 m Liverpool Telescope (LT) at La Palma. Near-infrared (NIR) photometric observations were obtained with NOTCAM on the 2.6 m Nordic Optical Telescope (NOT) at La Palma and WFCAM mounted on the 3.8 m United Kingdom Infra-Red Telescope (UKIRT) at Maunakea. We also triggered near-ultraviolet (NUV) observations with the Neil Gehrels Swift Observatory (Gehrels et al. 2004) Ultraviolet/Optical telescope (UVOT). For optical and NIR data, point-spread-function (PSF) pho-

tometry was performed using a PyRAF-based pipeline¹ employing standard DAOPHOT-IRAF photometry packages. The PSF radius and sky annulus were selected based on the mean full width at half-maximum intensity (FWHM) of stellar profiles for each image frame. Optical photometric calibration was done using SDSS (for the *g*, *r* and *i* bands; SDSS Collaboration et al. 2017) and APASS DR9 (for the *B* and *V* bands; Henden et al. 2016) catalogues of stars in the field. 2MASS (Skrutskie et al. 2006) local standards were used to calibrate the NIR photometry. No host-galaxy subtraction has been done for the optical or NIR data, as the SN is located outside the optical disk of the host and the contamination is negligible during our observed epochs. The UVOT photometry was performed with the UVOTSOURCE task in the HEASoft package using an aperture of $5''$ radius and placed in the Vega magnitude system, using the calibration from Breeveld et al. (2011). UVOT templates images observed at +426 d were used to subtract the host-galaxy contamination in the lower resolution *Swift* images. The photometric data for ASASSN-18am are in Table 1. The uncertainties from the PSF photometry, differential photometry, and zero-point calibration are all propagated into the final reported uncertainties.

We obtained 17 optical spectra spanning from 2 to 218 days (in the observer’s frame) after discovery. Long-slit spectroscopic observations were carried out using the FAST spectrograph (Fabricant et al. 1998) mounted on 1.5 m Tillinghast telescope at the F. L. Whipple Observatory (AZ, USA), ALFOOSC on the 2.6 m NOT at La Palma, the Kast double spectrograph mounted on the 3 m Shane telescope at Lick Observatory (CA, USA), LRIS (Oke et al. 1995) on the 10 m Keck-I telescope at Maunakea (HI, USA), the Double Spectrograph (DBSP) on the 5 m Hale Telescope at Palomar Observatory (CA, USA), BFOOSC mounted on the Xing-long 2.16 m telescope of the National Astronomical Observatories (CAS, China), OSMOS (Martini et al. 2011) on the 2.4 m Hiltner Telescope at MDM Observatory (AZ, USA), OSIRIS on the 10.4 m Gran Telescopio Canarias (GTC) at La Palma (Spain), and MODS (Pogge et al. 2010) on the twin 8.4 m LBT at Mount Graham International Observatory (AZ, USA). Spectra are obtained with the slit along the parallactic angle (Filippenko 1982) in order to obtain accurate relative spectrophotometry. The Keck/LRIS spectrum was taken with an atmospheric dispersion compensator.

The medium-resolution spectra from MODS were reduced using the modsIDL pipeline, and the ALFOOSC data using ALFOOSCGUI². The DBSP, OSMOS, and OSIRIS data were reduced with PyRAF-based SimSpec³ pipeline. The standard FAST pipeline was used for the FAST spectra, with Massey standards (Massey & Gronwall 1990) for spectrophotometric calibration. The LRIS spectrum was reduced using the IDL-based LPipe pipeline (Perley 2019), and the BFOOSC spectra were reduced using standard IRAF routines. Kast data were reduced following standard techniques for CCD processing and spectrum extraction utilising IRAF routines and custom Python and IDL codes⁴. The spectroscopic observations are summarised in Table 2.

ASASSN-18am was observed in photon-counting mode with the *Swift* X-ray Telescope (XRT; Burrows et al. 2005) from 2018-01-21 (+9 d) to 2018-03-06 (+52 d) for a total exposure time of 35.2 ks. The SN was also observed by the *Chandra* X-ray Observatory on 2018-04-21 (+60 d) with a 10 ks exposure. Source

¹ <https://astro.subhashbose.com/software/diffphot>

² <http://sngroup.oapd.inaf.it/foscgui.html>; developed by E. Cappellaro

³ <https://astro.subhashbose.com/simspec/>

⁴ <https://github.com/ishivvers/TheKastShiv>

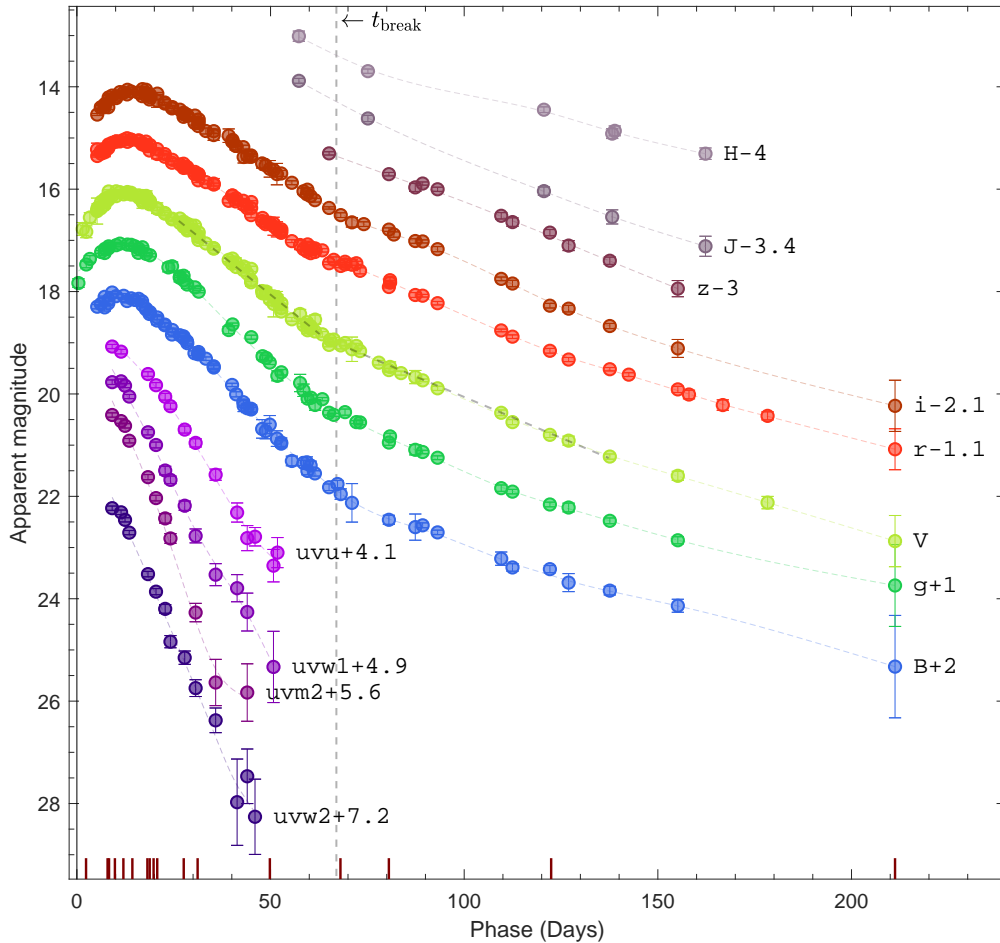


Figure 2. The photometric evolution of ASASSN-18am in the UVOT-NUV, optical *BVgriz*, and NIR bands. Epochs of spectral observations are marked by vertical bars at the bottom. The data points at day 211 are synthetic magnitudes computed from the spectrum taken at that epoch. A pair of lines (grey colour) are overplotted on the *V*-band light curve to help illustrate the break in its slope. The time of a break in the light-curve slope is shown by a grey vertical dashed line, t_{break} .

counts were extracted in a circle with a radius of $24''$. Background counts were selected from a nearby source-free circular region. The Galactic column density in the direction of ASASSN-18am is $N_H = 9.7 \times 10^{19} \text{ cm}^{-2}$ (Kalberla et al. 2005). The X-ray spectrum can be fit with a single absorbed power-law model with a photon index $\Gamma = 0.77^{+0.70}_{-0.75}$. Based on this model the count rates are converted into a $0.3 - 10 \text{ keV}$ flux. The X-ray detections and upper limits are listed in Table. 3.

There are two X-ray sources detected by the *Swift* XRT in the vicinity of the optical position of ASASSN-18am. The eastern one, which is also clearly detectable in the *Chandra* image, corresponds to a $z = 0.95$ quasar (WISEA J163556.97+400138.6). The astrometric position (J2000) of the other X-ray source is $\alpha = 16^{\text{h}}35^{\text{m}}53^{\text{s}}.89$, $\delta = +40^{\circ}01'58''.7$, with an uncertainty radius of $12''.3$ (90% confidence). This position is $2''.5$ away from the optical position of ASASSN-18am and is well within the uncertainty radius. Other than the SN, no other object is visible in the UVOT images at that X-ray position, and given that the optical position is within the extraction radius of the X-ray source we are confident that these are X-rays emerging from the supernova and not from a background object (such as the eastern source).

X-rays were only detected from +11 d to +14 d with luminosities in the range $\sim (4-6) \times 10^{41} \text{ erg s}^{-1}$. From +18 d onward, the

SN was no longer detected in the *Swift* observations. The *Chandra* observation at +60 d also could not detect any emission down to a limit of $3.8 \times 10^{40} \text{ erg s}^{-1}$.

4 LIGHT CURVE

Figure 2 shows the NUV, optical, and NIR light curves of ASASSN-18am. We estimate a rise-to-peak time of $12.3 \pm 4.6 \text{ d}$ for the *V*-band light curve by fitting a third-order polynomial. This rise time is similar to that of some fast declining SNe IIP/L (e.g., SN 2013ej, Valenti et al. 2014; SN 2014G, Bose et al. 2016). After the peak, the optical light curves decline monotonically, and can be basically described by two-piece linear (in mag) components with a break near 65 d (shown by a vertical dashed line, t_{break}). The early-time (20–65 d) light-curve decline rates are 17.1 (*uvw2*), 21.0 (*uvw2*), 14.1 (*uvw1*), 11.4 (*uvu*), 7.5 (*B*), 6.9 (*g*), 6.0 (*V*), 4.9 (*r*), and 4.9 (*i*) $\text{mag} (100 \text{ d})^{-1}$ for each band. The decline rates during this photospheric phase are significantly steeper than those of normal SNe II, including the fast-declining SNe IIL (see, e.g., Bose et al. 2016). After the break near day 65, the light curve settles onto a slower declining tail until the end of our photometric observations at 178 d. The slopes of this tail phase are 2.4 (*B*), 2.7 (*g*), 2.9 (*V*), 2.8 (*r*), 3.2 (*i*), 3.0 (*z*), 2.9 (*J*), and 1.9 (*H*) $\text{mag} (100 \text{ d})^{-1}$ for each

band. These decay rates are significantly steeper than for a fully γ -ray-trapped $^{56}\text{Ni} \rightarrow ^{56}\text{Co} \rightarrow ^{56}\text{Fe}$ powered light curve with a slope of $0.98 \text{ mag } (100 \text{ d})^{-1}$.

4.1 Absolute magnitude and bolometric luminosity and NIR colour

The peak V -band absolute magnitude of ASASSN-18am is $M_{V,\text{peak}} = -19.70 \pm 0.27 \text{ mag}$, which lies between that of typical ccSNe and SLSNe, making ASASSN-18am one of the small number of LSNe-II discovered thus far. In Figure 3 we compare the absolute V -band light curve of ASASSN-18am with a sample of SNe II comprised of normal SNe IIP/L, SNe IIb, and LSNe-II having peak absolute magnitudes similar to that of ASASSN-18am. The peak absolute magnitude of ASASSN-18am is brighter by $\sim 1.4 \text{ mag}$ than the brightest of the normal SNe II (e.g., SN 1980K, 2013by, and 2014G), all of which are also fast-declining SNe IIL. The early-time light curve of ASASSN-18am has a faster decline rate than any SN in the comparison sample. For example, among the normal SNe II, SN 1980K has one of the fastest V -band photospheric-phase decline rates of $\sim 3.9 \text{ mag } (100 \text{ d})^{-1}$, while ASASSN-18am declines at $6.0 \text{ mag } (100 \text{ d})^{-1}$.

ASASSN-18am exhibits a break in its light-curve slope at $\sim 65 \text{ d}$ and thereafter settles onto a relatively slowly declining tail phase. Unlike normal SNe II, which always show a drop of few magnitudes during the transition at $\sim 100 \text{ d}$ from the photospheric to the radioactive-decay phase, ASASSN-18am does not have any such feature. ASASSN-15nx is another LSN-II lacking this transition phase, but it differs from ASASSN-18am by having a continuous linear decline without any break demarcating the photospheric and the nebular phases. The tail light-curve decline rate of ASASSN-18am ($2.9 \text{ mag } (100 \text{ d})^{-1}$) is also significantly steeper than that expected from a light curve powered by fully γ -ray-trapped radioactive decay (slope $0.98 \text{ mag } (100 \text{ d})^{-1}$). However, its decline rate is comparable to that of other LSNe-II, such as ASASSN-15nx and also possibly SN 2016gsd.

In Figure 4 we compare the bolometric light curve of ASASSN-18am with that of other well-studied normal SNe and the LSN-II ASASSN-15nx. For ASASSN-18am, the bolometric luminosities are calculated by fitting a blackbody to the NUV and optical bands until 54 d. At later times, when NIR data (J and H bands) are available, we directly integrated over the SED, although blackbody models give very similar results (differences $\leq 0.05 \text{ dex}$). At 57 d, where we also have K -band data, we tested the blackbody model on the optical-NIR SED and found that the NIR fluxes are consistent with blackbody emission. For the direct integration of the SED, we assumed zero flux beyond 2000 \AA and extrapolated the H -band flux assuming a Rayleigh-Jeans approximation. The NUV contribution to the bolometric luminosity becomes negligible after $\sim 25 \text{ d}$. The bolometric light curve comparison shows trends similar to those for the absolute magnitudes, where the two LSNe-II ASASSN-18am and ASASSN-15nx are roughly 1.5 dex brighter near maximum than typical ccSNe.

The H -band decline rate (see Fig. 2) is significantly slower than all other bands (from B through J), suggesting an excess in the H -band flux. In Figure 5 we compare the extinction-corrected $(i-H)_0$ NIR colour with a sample of SNe II and SNe IIb. SN 2006jc (Ibn; Mattila et al. 2008; Pastorello et al. 2008) and SN 2010jl (IIc; Fransson et al. 2014) are also included for comparison; they have strong IR excesses as a manifestation of dust emission. Until $\sim 80 \text{ d}$, ASASSN-18am has a NIR colour similar to that of other SNe, and then it becomes significantly redder at later times. Owing to the lack

of data redder than the H band, the exact reason for the reddening is unclear. One possibility is the presence of some strong emission line in the H band, or alternatively IR emission from warm dust. SNe can show IR emission from dust at longer wavelengths during late times (e.g., SN 1987A, Bouchet & Danziger 1993, and references therein; SN 2004dj, Meikle et al. 2011; SN 2004et Maguire et al. 2010; Kotak et al. 2009; SN 2011dh Ergon et al. 2015; and ASASSN-16at Bose et al. 2019). SNe 2006j and 2010jl also showed strong excesses of flux in H which were explained by IR emissions from dust (Mattila et al. 2008; Fransson et al. 2014).

5 SPECTRA

Figures 6 and 7 show the spectral evolution of ASASSN-18am. Figure 6 displays the first 18 d where the spectra are predominantly a featureless blue continuum. ‘‘Flash-ionisation’’ features are seen only in the earliest spectrum. The spectroscopic evolution from day 18 until the nebular phase is shown in Figure 7.

5.1 Flash ionisation and blue continuum

The earliest +2.4 d spectrum reveals narrow emission lines of H and ionised He on top of a blue continuum. These features originate from the recombination of CSM that was flash ionised by the initial shock-breakout radiation pulse (see, e.g., Niemela et al. 1985; Gal-Yam et al. 2014). The emission-line profiles of $H\alpha$ and He II $\lambda 4686$ can be described by a combination of a broad Lorentzian and narrow Gaussian components, but the $H\beta$ and He II $\lambda 5411$ profiles can be described by a single broad component; the narrow component cannot be detected in our low-resolution spectra. Such extended wings can be created by the radiative acceleration of the CSM by the shock-breakout luminosity (e.g., Kochanek 2019). Additionally, electron scattering can contribute to the formation of these extended wings (e.g., Fransson et al. 2014). The measured FWHMs of the $H\alpha$ profile are $2879 \pm 553 \text{ km s}^{-1}$ and $206 \pm 61 \text{ km s}^{-1}$ for the broad and narrow components (respectively), and $12,784 \pm 1236 \text{ km s}^{-1}$ and $876 \pm 110 \text{ km s}^{-1}$ for the broad and narrow components (respectively) of He II $\lambda 4686$. However, the FWHM of the narrow component of $H\alpha$ is limited by the instrumental resolution of the FAST spectrograph and should be considered an upper limit. For $H\beta$ and He II $\lambda 5411$, the respective measured FWHMs for the broad components are $3319 \pm 1266 \text{ km s}^{-1}$ and $7971 \pm 1660 \text{ km s}^{-1}$.

The next spectrum, obtained at +7.9 d, lacks any flash-ionisation features, leaving a blue and featureless continuum that lasts until +18.2 d. We continued spectroscopy at a relatively higher cadence to constrain when emission lines start to appear. It was only 0.6 d between the last featureless spectrum (+18.2 d) and the appearance of spectral lines (+18.8 d), though the +18.2 d spectrum has significantly lower signal-to-noise ratio than the +18.8 d spectrum. The presence of a blue continuum with or without the flash-ionisation features in the first 2–18 d indicates a hot, optically thick envelope with temperatures of $\sim 11,000 \text{ K}$ to $\sim 15,000 \text{ K}$. From a study of a sample of early-time SN II spectra, Khazov et al. (2016) suggested that flash-ionisation lines and featureless blue continua are more common in higher luminosity SNe, although none of the SNe in their sample is as luminous as ASASSN-18am. Khazov et al. (2016) also found that all flash-ionisation features in their sample are in spectra of age $< 10 \text{ d}$. ASASSN-18am is the only LSN-II having such early-time spectra. The earliest spectra of the well-studied LSNe-II PTF10iam (Arcavi et al. 2016) and SN 2013fc (Kangas et al. 2016) were taken at $\sim 15 \text{ d}$ and show only a blue featureless

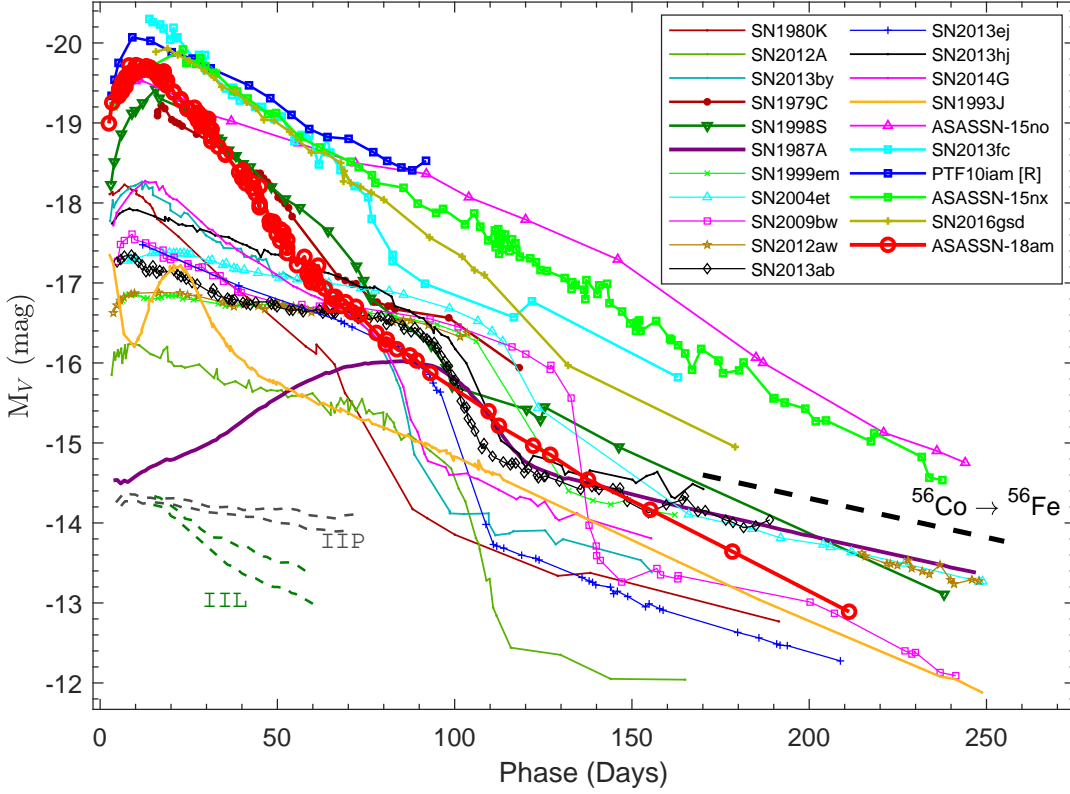


Figure 3. The absolute V-band light curve of ASASSN-18am compared with other normal and luminous H-rich SNe. The slope for a $^{56}\text{Co} \rightarrow ^{56}\text{Fe}$ radioactive decay law with full γ -ray trapping is shown with a thick black dashed line. On the bottom-left side, pairs of grey and green dashed lines show the slope range for the SN II-P and SN II-L templates given by [Faran et al. \(2014\)](#). The adopted explosion time in JD $- 2, 400, 000$, distance in Mpc, total $E(B - V)$ in mag, and references for the light curves are as follows. SN 1979C – 43970.5, 16.0, 0.31, [Barbon et al. \(1982b\)](#); [de Vaucouleurs et al. \(1981\)](#); SN 1980K – 44540.5, 5.5, 0.30, [Barbon et al. \(1982a\)](#); SN 1987A – 46849.8, 0.05, 0.16, [Hamuy & Suntzeff \(1990\)](#); SN 1999em – 51475.6, 11.7, 0.10, [Leonard et al. \(2002\)](#); [Elmhamdi et al. \(2003\)](#); SN 2004et – 53270.5, 5.4, 0.41, [Sahu et al. \(2006\)](#); SN 2009bw – 54916.5, 20.2, 0.31, [Inserra et al. \(2012\)](#); SN 2012A – 55933.5, 9.8, 0.04, [Tomasella et al. \(2013\)](#); SN 2012aw – 56002.6, 9.9, 0.07, [Bose et al. \(2013\)](#); SN 2013ab – 56340.0, 24.0, 0.04, [Bose et al. \(2015a\)](#); SN 2013by – 56404.0, 14.8, 0.19, [Valenti et al. \(2015\)](#); SN 2013ej – 56497.3, 9.6, 0.06, [Bose et al. \(2015b\)](#); SN 2013hj – 56637.0, 28.2, 0.10, [Bose et al. \(2016\)](#); SN 2014G – 56669.7, 24.4, 0.25, [Bose et al. \(2016\)](#); ASASSN-15no – 57235.5, 153.5, 0.045, [Benetti et al. \(2018\)](#); SN 1993J – 9074.0, 3.68, 0.069, [Richmond et al. \(1996\)](#); PTF10iam – 55342.7, 453.35, 0.19, [Arcavi et al. \(2016\)](#); SN 2013fc – 56516.7, 83.2, 0.935, [Kangas et al. \(2016\)](#); ASASSN-15nx – 57219.1, 127.5, 0.07, [Bose et al. \(2018\)](#); and SN 2016gsd – 57648.5, 311.6, 0.08, [Reynolds et al. \(2020\)](#).

continuum. For other LSNe-II, such as ASASSN-15nx ([Bose et al. 2018](#)) and SN 2016gsd ([Reynolds et al. 2020](#)), spectra were obtained only after > 23 d and already exhibit broad emission lines.

Under the assumption that the $\text{H}\alpha$ emission in the first spectrum is due to recombination of CSM photoionised by the shock-breakout radiation, we can estimate the wind mass-loss rate. For this order-of-magnitude estimate, we will ignore the extra complications caused by light-travel time effects (see [Kochanek 2019](#)). The $\text{H}\alpha$ recombination luminosity of a fully ionised hydrogen wind is

$$L_{\text{H}\alpha} = \frac{\dot{M}^2 \alpha_{\text{H}\alpha} \epsilon_{\text{H}\alpha}}{4\pi v_w^2 m_p^2 R_{\text{in}}}, \quad (1)$$

where \dot{M} is the mass-loss rate, $\alpha_{\text{H}\alpha} \approx 1.2 \times 10^{-13} \text{ cm}^3 \text{ s}^{-1}$ is the Case B $\text{H}\alpha$ recombination rate, m_p is the proton mass, and $\epsilon_{\text{H}\alpha} = 1.8 \text{ eV}$. The inner edge of the wind is $R_{\text{in}} \approx R_* + v_s t \approx 2 \times 10^{14} \text{ cm}$ assuming a stellar radius of $R_* = 500 R_\odot$ and a shock speed of $v_s = 10^4 \text{ km s}^{-1}$. The mass-loss rate depends little on the assumed radius R_* once $v_s t \gg R_*$. We assume a typical wind velocity of $v_w = 30 \text{ km s}^{-1}$ since the observed line FWHM $\approx 200 \text{ km s}^{-1}$ is limited by the instrumental resolution. Given the observed luminosity of $L_{\text{H}\alpha} = 9.8 \times 10^{38} \text{ erg s}^{-1}$, we can solve for

the required mass-loss rate as

$$\dot{M} \approx 1.4 \left[\frac{L_{\text{H}\alpha}}{10^{39} \text{ erg s}^{-1}} \cdot \frac{R_{\text{in}}}{10^{14} \text{ cm}} \right]^{1/2} \left[\frac{v_w}{30 \text{ km s}^{-1}} \right] \times 10^{-4} M_\odot \text{ yr}^{-1}, \quad (2)$$

or $\dot{M} \approx 2 \times 10^{-4} M_\odot \text{ yr}^{-1}$ for our nominal values.

In the presence of density inhomogeneities, the actual mean wind density will be lower than estimated from the recombination luminosity. By the time of the second spectrum on day 7.9, the inner radius would have expanded to $R_{\text{in}} \approx 7 \times 10^{14} \text{ cm}$ and we would expect the CSM emission to have dropped by a factor of three. Combined with the increased continuum flux, it makes the nondetection of flash-ionisation features in this second spectrum plausible.

5.2 Evolution of key spectral features

Figure 7 shows the appearance and evolution of the spectral lines in ASASSN-18am. At day 18.8, only 0.6 d after the last featureless spectrum, broad P-Cygni profiles of $\text{H}\alpha$, $\text{He I } \lambda 5876$, and $\text{H}\beta$ begin to appear and steadily strengthen. Lines of intermediate-mass and

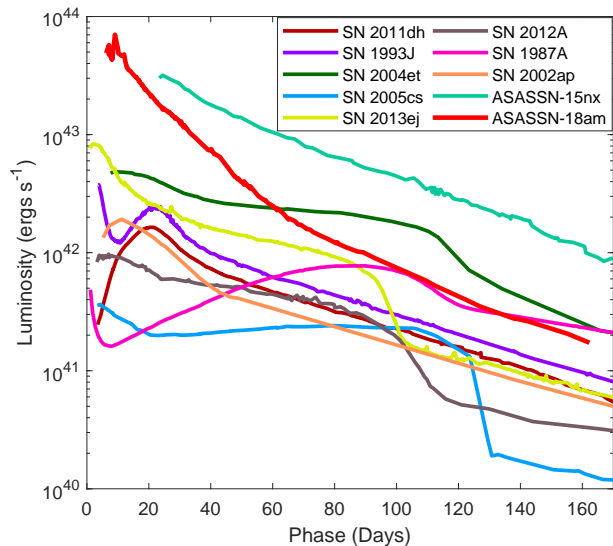


Figure 4. The bolometric light curve of ASASSN-18am compared with those of ASASSN-15nx (LSN II; Bose et al. 2018), SN 2011dh (Ib; Ergon et al. 2015), SN 1993J (Ib; Richmond et al. 1996), SN 2004et (II; Sahu et al. 2006), SN 2005cs (II; Pastorello et al. 2006, 2009), SN 2013ej (II; Yuan et al. 2016), SN 2012A (II; Tomasella et al. 2013), SN 1987A (II; Hamuy & Suntzeff 1990), and SN 2002ap (Ic-BL; Yoshii et al. 2003). Comparison light curves for the normal-luminosity SNe are from Sharon & Kushnir (2020).

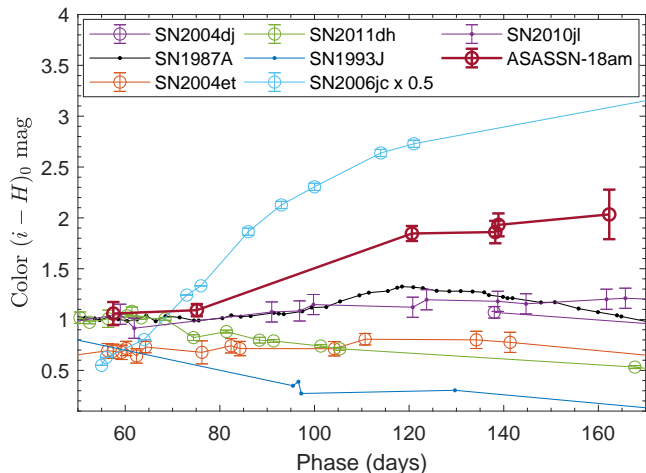


Figure 5. The extinction-corrected $(i - H)_0$ optical-to-NIR colour of ASASSN-18am is compared with that of other SNe II. SN 2006jc (Ibn) and SN 2010jl (II_n) are also included for comparison. For clarity, the colour curve of SN 2006jc is scaled down to half of its values.

iron-group elements also appear after the +31 d spectrum and persist until the last epoch of observation at +211 d.

Forbidden emission lines of [O I] $\lambda\lambda 6300, 6364$ and [Ca II] $\lambda\lambda 7291, 7324$, which are characteristic nebular-phase features, become prominent from +80.6 d onward. During the nebular phase (> 80 d), the most dramatic evolution is seen at ~ 6000 – 7000 Å. The apparent $H\alpha$ emission becomes relatively weak compared to the metal lines, while the [O I] emission grows substantially stronger at +122.5 d and is the dominant emission feature in the +211.2 d spectrum. During the nebular phase, the He I emission component becomes stronger but it is blended with the weak

$H\alpha$ emission, as identified in the `synow` models at earlier phases (see below). The weak and unresolved $H\alpha$ emission in the nebular phase indicate a low hydrogen content in the ejecta. In the late-time spectrum at +211.2 d, the broad feature is predominantly [O I] emission, while the extended blue wing is likely a blend of He I and [N II] $\lambda\lambda 6548, 6583$. This spectral feature is reminiscent of the nebular-phase spectra of SNe IIB or SNe Ib.

We used `synow` (Branch et al. 2002; Fisher et al. 1997) to model the spectra and identify lines using a set of atomic species H I, He I, O I, Fe II, Ti II, Sc II, Ca II, and Ba II. The models with the line identifications at three different phases are shown in Figure 8. Although `synow` is only suitable for modeling spectra during the photospheric phase, we also modeled the +122.5 d spectrum, as it has only partly transitioned to the nebular phase; P-Cygni profiles are still visible with a photospheric velocity of ~ 6500 km s $^{-1}$.

In comparison to normal SNe II, ASASSN-18am has more complex blends of lines, especially on the blue side of the spectrum (< 5500 Å), which the `synow` models cannot fully reproduce. However, we could identify the dominant species, among which the He I lines are one of the most important identifications. In spectra older than a few weeks, the strong absorption profiles near 5700 Å are generally attributed to Na I D $\lambda\lambda 5890, 5896$ in H-rich SNe IIP/L. However, this line is also very close to He I $\lambda 5876$ which is difficult to distinguish from Na I D when the line velocities are high. Nevertheless, in the +80.6 d and +122.5 d spectra of ASASSN-18am, we identify this line as He I instead of Na I D. Identified as He I, the line velocity is well aligned with all the other metallic line velocities as well as the photospheric velocity of the model, whereas fitting the feature as Na I D would require a $\sim 30\%$ (~ 2000 km s $^{-1}$) higher velocity than the photosphere. Moreover, by invoking He I as the identification, we could also reproduce two additional absorption features — one at ~ 6900 Å (He I $\lambda 7065$) and the other as a minor dip at ~ 6560 Å (He I $\lambda 6678$) near the top of apparent the $H\alpha$ emission — which further corroborates our line identification.

5.3 Spectroscopic comparison

In Figures 9 to 11 we compare the spectra of ASASSN-18am with those of other H-rich SNe, including the LSNe-II PTF10iam, SN 2013fc, ASASSN-15nx, and SN 2016gsd. In Figure 9 we compare the +68 d and +81 d spectra of ASASSN-18am with other SNe at similar phases. Overall, ASASSN-18am has many similarities to other SNe IIP/L. An $H\alpha$ profile with a weak absorption component is similar to that of other fast-declining SNe II such as SN 1979C and SN 1998S. However, the apparently broad $H\alpha$ profile near 6500 Å is identified as a blend of $H\alpha$ and He I in `synow`, and does not match the SN IIP/L spectra. The partially blended $H\alpha$ and He I profile of SN IIB 1993J is somewhat similar to that of ASASSN-18am, but the $H\alpha$ and He I lines are not distinctly resolved in the latter. This suggests that even if ASASSN-18am is spectroscopically a “SN IIB,” it is likely richer in hydrogen than typical SNe IIB.

In Figure 10 the early nebular spectrum of ASASSN-18am at 123 d is compared with a subset of the SNe from the previous figure. The Fe II and $H\beta$ lines near 4700 Å, the [Ca II] emission near 7300 Å, and the O I $\lambda 7774$ line are similar to the comparison sample. However, the line profiles in the range 6000–7000 Å are significantly different from those of the other SNe, with SN IIB 1993J being the closest match. This again seems to imply that the $H\alpha$ in ASASSN-18am is weaker than in SNe IIP/L or ASASSN-15nx, but stronger than in SN IIB 1993J. Strong [O I] $\lambda\lambda 6300, 6364$ emission is also seen in SNe 1993J and ASASSN-15nx, suggesting that these SNe

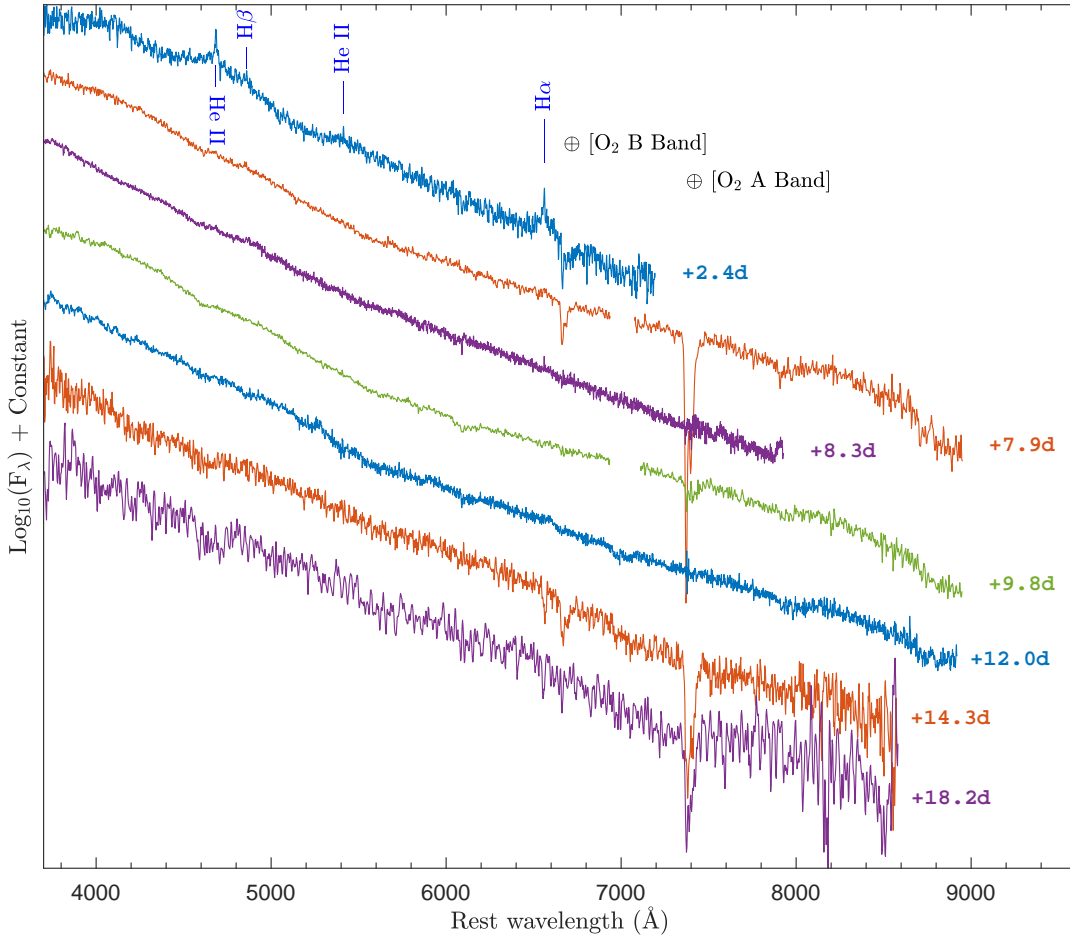


Figure 6. Spectral evolution of ASASSN-18am from 2 d to 18 d showing flash-ionisation features in the first spectrum and a blue featureless continuum in the remainder. The positions for telluric absorption features are marked with \oplus symbol; they were not removed from some spectra.

have relatively thin hydrogen envelopes and enter the nebular phase much earlier than their H-rich counterparts (SNe IIP/L).

The nebular-phase spectrum of ASASSN-18am at +211 d is compared with other ccSNe in Figure 11. The spectrum is again very similar to that of SN Iib 1993J, especially the broad and blended feature near 6300 Å which is formed by [O I], He I, and [N II]. Unlike the previous spectrum, H α is likely very weak or nonexistent at this phase and now [N II] has a stronger contribution (Jerkstrand et al. 2015). SN 2015bs, a SN II from a massive ($\sim 25 M_{\odot}$) progenitor (Anderson et al. 2018), is also included for comparison. It shows strong [O I] emission like ASASSN-18am but with additional, prominent H α emission. Typical SNe II (e.g., SN 2012aw) and the LSN-II ASASSN-15nx show much weaker [O I] emission. We also included two SNe Ic-BL, SN 1998bw (Patat et al. 2001) and SN 2002ap (Foley et al. 2003), for comparison. The blue (4300–6000 Å) spectra of ASASSN-18am are remarkably similar to these SNe Ic-BL. Two notable similarities are the prominent blends of Mg I λ 4750, [Fe III] λ 4658, and [Co II] λ 4624 near 4600 Å, and the blends of [Fe III] λ 5270 and [Fe II] multiplets near 5200 Å (see Mazzali et al. 2007 for the line identifications). Such strong lines of iron-group elements are not seen in other SNe II. The emission feature near 5900 Å resembles the Na I D λ 5890, 5896 doublet commonly seen in ccSNe nebular spectra. In earlier phases the same region is dominated by He I. However, owing to the presence of relatively strong iron-group lines, we also expect

some contribution from [Co III] λ 5888 emission in this feature. We measure the flux ratio between the 123 d and 211 d spectra to be $\sim 7.5 \pm 0.5$, while for pure cobalt decay it is expected to be ~ 10.4 (Childress et al. 2015). This re-affirms that the 5900 Å feature at these phases is dominated by Na I D or weak He I emission.

5.4 Line velocities

In Figure 12 we show the H α , H β , He I, and Fe II line-velocity evolution defined by the minimum of the absorption feature. Broad P-Cygni profiles of H α , H β , and He I start to appear from +18.8 d with high expansion velocities ($\sim 17,000 \text{ km s}^{-1}$ for H α). Since this spectrum was only 0.6 d after the last blue, featureless spectrum, the lines are likely formed very close to the outermost layer of the ejecta at high velocities. Over the first three epochs to +20.7 d the velocities drop rapidly, and afterward they decline slowly. After +49.8 d, the H α and H β velocities remain almost constant at $\sim 10,000 \text{ km s}^{-1}$ and $\sim 8500 \text{ km s}^{-1}$, respectively. The flat velocity profiles indicate a stratified shell of H I with little or no mixing in the ejecta. The highest He I velocity of $\sim 11,000 \text{ km s}^{-1}$ is roughly at the lower bound of the H α velocity. This suggests that, although H I is mostly confined to a shell, it is not detached from the He I core.

We compare the H α , H β , and Fe II/He I line velocities with a sample of other SNe II in Figure 13. The Fe II lines represent the photospheric velocity, and during early phases (+18.8 d to +20.7 d

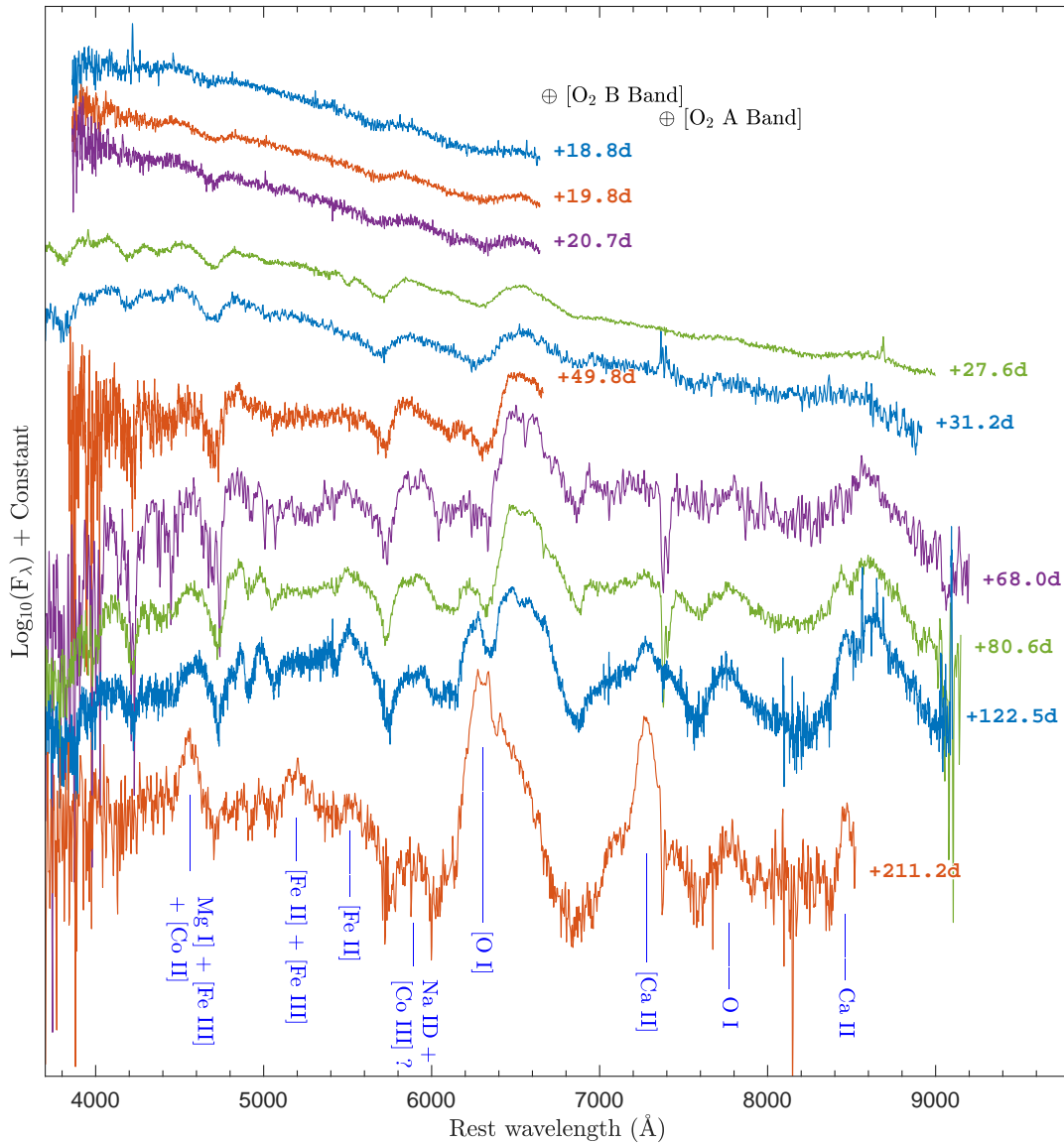


Figure 7. Spectral evolution of ASASSN-18am from 19 d to 211 d showing the emergence and evolution of the spectral lines. The positions for telluric absorption features are marked with \oplus symbol.

for ASASSN-18am) when Fe II lines are not detectable the He I lines are a good proxy for photospheric velocity (Takáts & Vinkó 2006; Bose & Kumar 2014). The comparison sample includes normal SNe II with prominent plateaus (IIP; e.g., SNe 2004et, 1999em, 2012aw), fast-declining SNe II (IIL; e.g., SN 2014G), intermediate decline rate SNe II (e.g., SN 2013ej), and ASASSN-18am-like LSNe-II (e.g., ASASSN-15nx, SN 2016gsd). SNe ASASSN-18am and 2016gsd are among those with highest velocities, and their velocities are significantly higher than those seen in normal SNe II. The earliest $H\alpha$ velocity of ASASSN-18am at $\sim 17,000 \text{ km s}^{-1}$ is larger than for any other object both in our sample and in the 122 SNe II analysed by Gutiérrez et al. (2017) where the maximum $H\alpha$ velocity is $\sim 15,000 \text{ km s}^{-1}$. SNe with faster light-curve declines tend to show flatter and overall higher H I velocity evolution curves (Faran et al. 2014; Bose et al. 2015b) as compared to SNe with more slowly declining light-curves. A similar trend is seen in Figure 13, with the exception of ASASSN-15nx. ASASSN-18am is the steepest declining SN II, followed by SNe 2016gsd, 2014G, 2013ej, and

then the rest of the SNe IIP with slowly declining or nearly flat light curves.

6 LIGHT CURVE AND ITS POWERING MECHANISM

The peak luminosity of ASASSN-18am is about an order of magnitude higher than that of typical SNe II. This makes it challenging to explain its powering mechanism. It is also one of the fastest declining SNe II, with a decline rate of $6.0 \text{ mag } (100 \text{ d})^{-1}$. Here we discuss some theoretical models and their limitations. We fit the models to the bolometric light-curve computed in §4.1.

6.1 Simple radiative diffusion

Here we use semi-analytical models with adiabatically expanding ejecta combined with radioactive heating and undergoing diffusion cooling as originally outlined by Arnett (1980) and Arnett & Fu

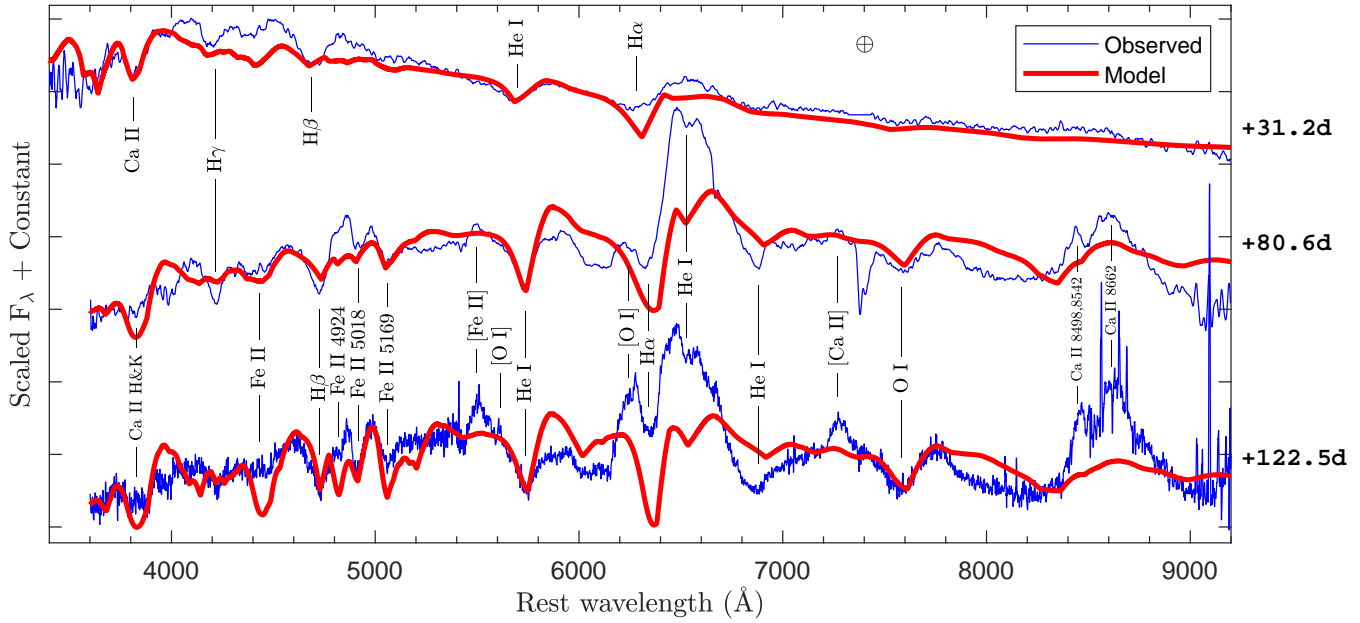


Figure 8. The *SYNOW* models and line identifications for ASASSN-18am at three epochs. The observed spectra are corrected for extinction and redshift. All prominent permitted lines are labeled by marking the corresponding absorption component except for Ca II $\lambda\lambda 8498, 8542, 8662$, while the emission peaks of forbidden lines are marked. Forbidden lines were identified by referring to previous identifications in the literature. Note that telluric absorption was not removed from the +80.6 d spectrum.

(1989). We first tried a single-component implementation of the model as described by Bose et al. (2015b). This model is unable to reproduce the steepness of the light curve earlier than ~ 30 d. Therefore, we extend this into a two-component ejecta model, where the core and a less massive envelope are treated independently, and the ^{56}Ni is confined to the core. This two-component formulation follows an approach similar to that of Nagy & Vinkó (2016); however, the implementation of the radioactive energy-deposition function is slightly different. We accurately account for the positron energy deposition from ^{56}Co decay and also ensure that the loss due to γ -ray leakage applies only to the ^{56}Ni heating and not to the radiated component of internal energy. These factors are important for steeply declining light curves having significant γ -ray leakage. This best-fit model is shown with a solid green line in Figure 14. In this model, the ejecta become optically thin by ~ 80 d, and thereafter the tail is entirely powered by radioactive decay.

The best-fit model has a radioactive ^{56}Ni mass of $M_{\text{Ni}} = 0.43 \pm 0.06 M_{\odot}$ with a γ -ray trapping parameter of $t_{0\gamma} = 53 \pm 7$ d, where $t_{0\gamma}$ defines the time-dependent γ -ray optical depth as $\tau_{\gamma} \approx r_{0\gamma}^2 / r^2$ (Jeffery 1999). The radioactive decay power alone cannot account for the radiated energy. The model has an total ejecta mass of $3 - 4 M_{\odot}$ with a very large kinetic energy $E_{\text{kin}} = (7-10) \times 10^{51}$ erg, and most of the energy is carried by the $\sim 1.5 M_{\odot}$ envelope. This large kinetic energy is consistent with the high expansion velocities measured from spectra (see §5.4). The large derived ^{56}Ni mass and high kinetic energy are also consistent with the empirical correlation for ccSNe found by Kushnir (2015a, see their Fig. 3).

We also estimated the ^{56}Ni parameters using the time-weighted luminosity integral method that conserves the energy considering adiabatic losses (Katz et al. 2013; Nakar et al. 2016; Sharon & Kushnir 2020) and found $M_{\text{Ni}} = 0.43 \pm 0.05 M_{\odot}$ with $t_{0\gamma} = 51 \pm 4$ d. The corresponding “ET” value is $(8 \pm 1) \times 10^{55}$ ergs, which is the excess energy released (time-weighted integral) in the ejecta without

the radioactive energy deposition. The derived M_{Ni} and $t_{0\gamma}$ values are identical to those estimated from direct fitting of the radioactive energy deposition function used for the radiative diffusion model.

6.2 Magnetar spin-down

A second possible powering mechanism is the spin-down of a newly formed magnetised neutron star, thereby injecting additional energy into the ejecta. Such magnetar engines can produce SN light curves with a wide range of luminosities depending on the spin period and the strength of the magnetic field (e.g., Kasen & Bildsten 2010). Magnetars are often discussed as a plausible powering mechanism for superluminous SNe (e.g., Nicholl et al. 2017; Dessart & Audit 2018). A magnetar engine was also proposed as a possible powering source for the LSN-II ASASSN-15nx (Chugai 2019). A central magnetar engine can lead to bipolar geometry for the SN ejecta (e.g., Sobacchi et al. 2017), which can be seen as an asymmetry in the nebular emissions lines, like in [O I]. Such features are not seen for ASASSN-18am, but this could simply be due to the viewing angle.

For the best-fit magnetar model (see Fig. 14, dark-yellow line) the progenitor at the time of explosion has an envelope mass of $\sim 2 M_{\odot}$ and the kinetic energy of the explosion is $E_{\text{kin}} = 3 \times 10^{51}$ erg. The estimated mass of ^{56}Ni synthesised in the explosion is $0.28 M_{\odot}$ with a γ -ray trapping parameter of $t_{0\gamma} = 122$ d. The central magnetar is estimated to have a magnetic field of $B = 4 \times 10^{15}$ gauss and an initial spin period of 1.2 ms. The magnetar properties needed to adequately reproduce the steep and luminous light curve are fairly extreme, but within theoretical limits (see, e.g., Gompertz et al. 2013). The estimated B value is higher than invoked for most models for SLSNe-I (Nicholl et al. 2017), and more consistent with magnetar powered long GRB models (Metzger et al. 2007). Thompson et al. (2004) suggested that a magnetar with such extreme

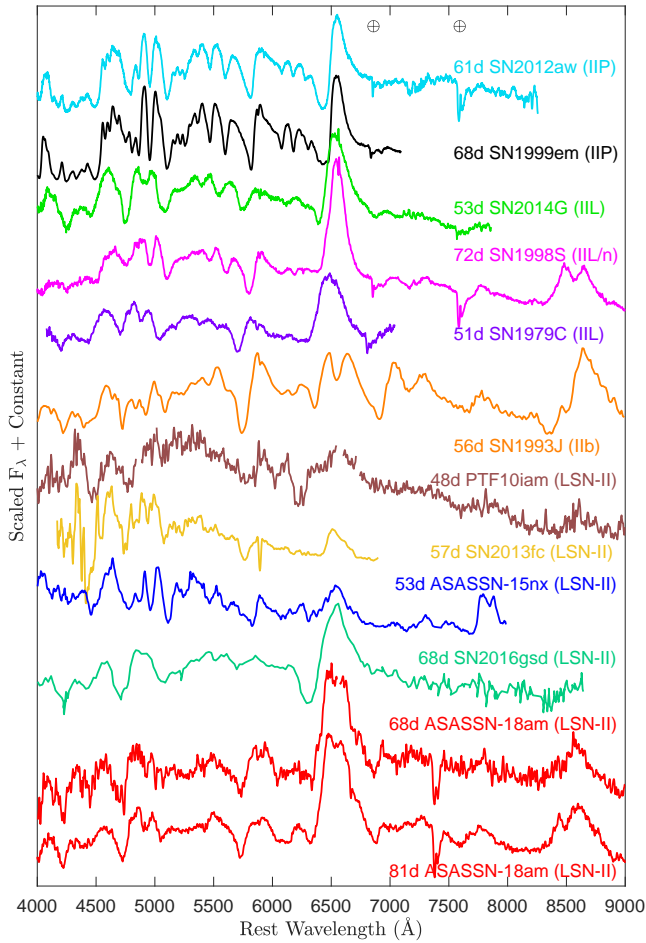


Figure 9. The 68 d and 81 d spectra of ASASSN-18am compared with spectra of other SNe. The name, type, and phase of the SNe are labeled in the figure. Luminous Type II SNe like ASASSN-18am are labeled as “LSNe-II.” The positions for telluric absorption features are marked with \oplus symbol.

parameters can spin down more rapidly than simple vacuum dipole spin-down, and that a rotational energy of up to $\sim 10^{52}$ erg can be extracted during first ~ 10 s after the birth of the protoneutron star, which may also significantly affect the SN shock dynamics.

6.3 Circumstellar interaction

Finally, we consider ejecta-CSM interaction as an alternative powering source for the luminous light curve of ASASSN-18am. One common example of ejecta-CSM interactions are SNe IIn, which are generally characterised by relatively narrow emission lines ($\text{FWHM} \approx 10^2\text{--}10^3 \text{ km s}^{-1}$) in their spectra (Schlegel 1990). Depending on the CSM density and wind-velocity profile, shock interactions can make SNe substantially more luminous, with a wide range of light-curve shapes. CSM interactions have been proposed for most of the LSNe-II to account for their high luminosities (e.g., SNe 2013fc Kangas et al. 2016; PTF10iam, Arcavi et al. 2016; ASASSN-15nx, Bose et al. 2018; and 2016gsd, Reynolds et al. 2020).

In ASASSN-18am, no relatively narrow lines are detected in the spectra after the first at +2.4 d. Nor do we see any other signatures proposed for CSM interaction scenarios contrived to hide

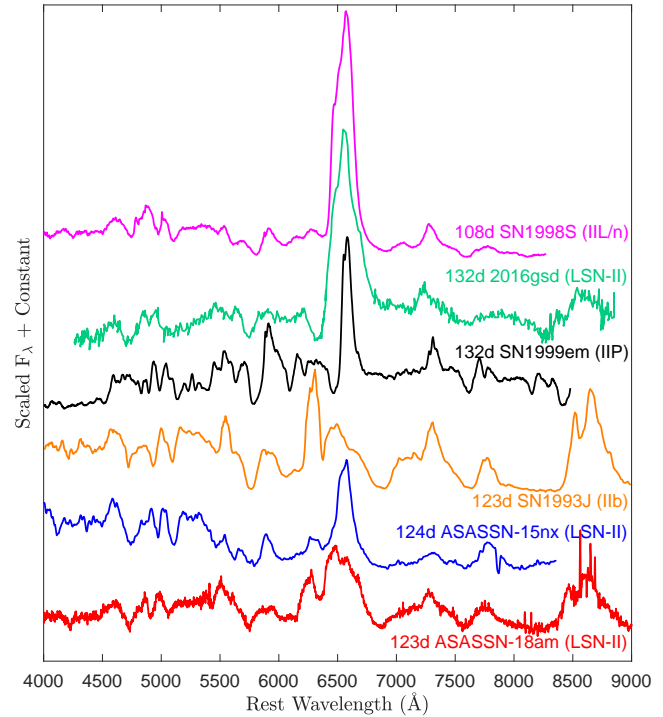


Figure 10. Same as Fig.9 but for the +123 d spectrum of ASASSN-18am.

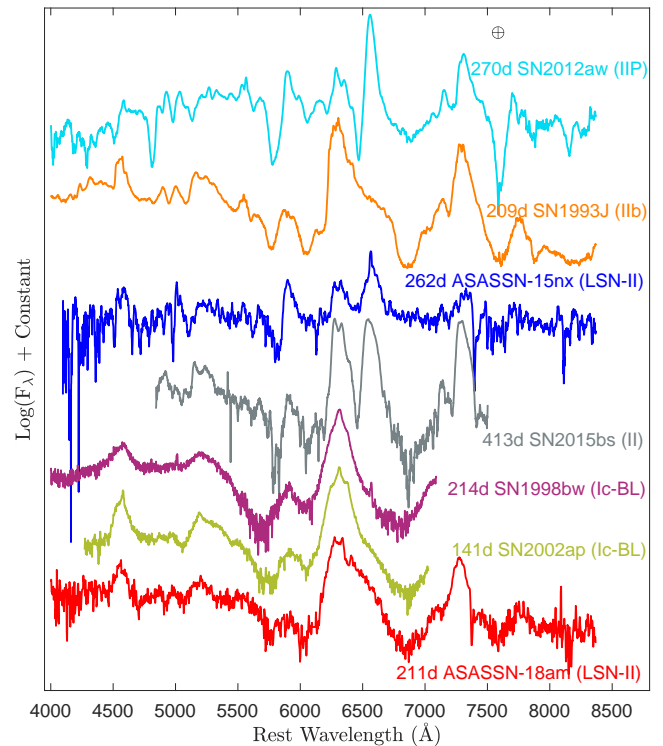


Figure 11. Same as Fig.9 but for the +211 d spectrum of ASASSN-18am and plotted on a logarithmic flux-density scale.

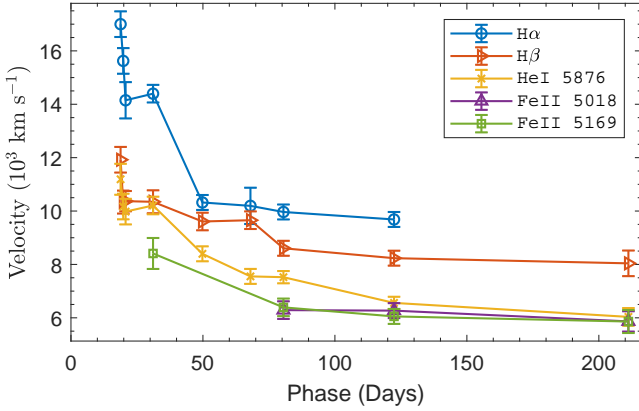


Figure 12. The velocity evolution of $H\alpha$, $H\beta$, $He\text{I}$, and $Fe\text{II}$ lines for ASASSN-18am.

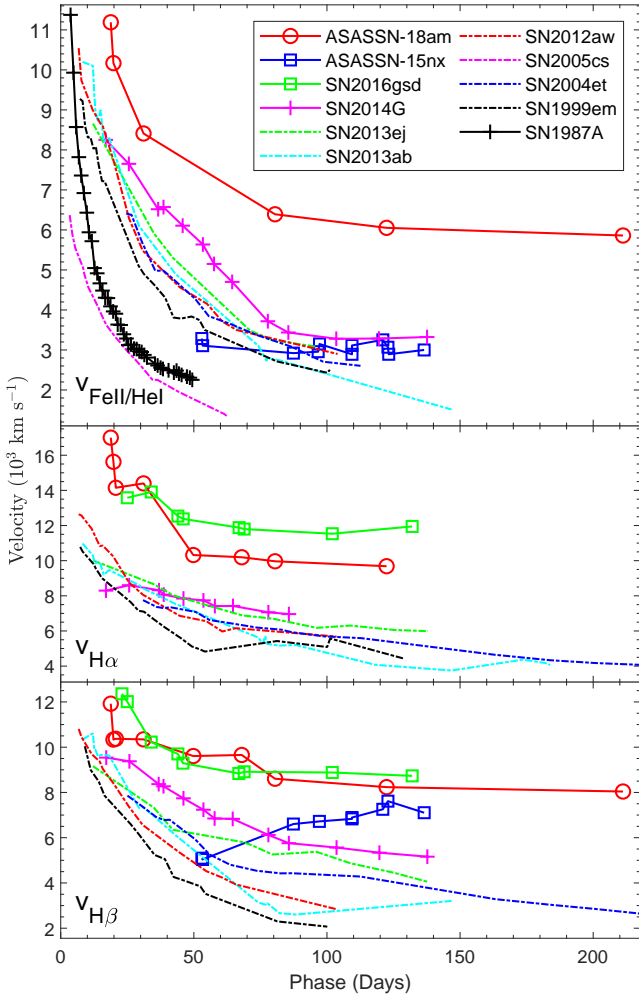


Figure 13. The top panel shows $Fe\text{II}$ line velocity profiles as a proxy for photospheric velocity. $He\text{I}$ velocities are subtitled in the profile when $Fe\text{II}$ lines are not detectable during early phases. The references for the sources of spectra are the same as for the light curves in Figs. 3 and 4, with the addition of Pun et al. (1995, SN 1987A) and Terreran et al. (2016, SN 2014G).

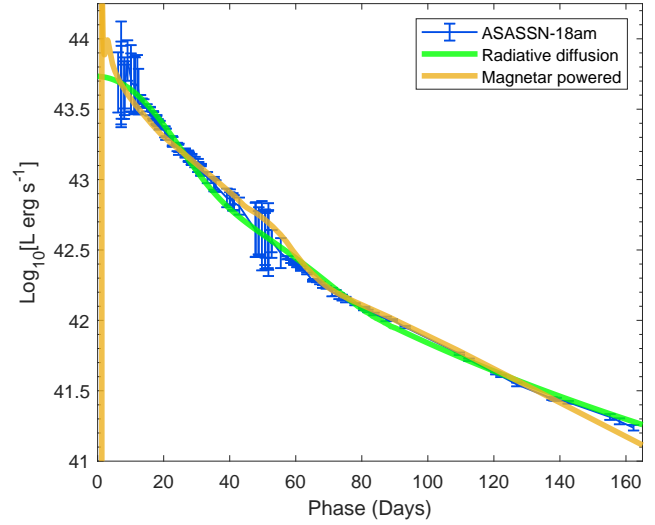


Figure 14. The light-curve fits of ASASSN-18am for the radiative diffusion and magnetar spin-down models.

narrow emission lines, like high-velocity $H\text{I}$ absorption components (see, e.g., Chugai 2007; Inserra et al. 2012; Bose et al. 2013, 2015b) or enhancement of the blue continuum (e.g., Chugai 2009; Smith et al. 2012; Bose et al. 2018). Using the flash-ionised lines in the first spectrum (see §5.1), we estimated a mass-loss rate of $\sim 2 \times 10^{-4} M_{\odot} \text{yr}^{-1}$, which is larger than for red supergiants ($\dot{M} \lesssim 10^{-4} M_{\odot} \text{yr}^{-1}$; e.g., de Jager et al. 1988; Beasor et al. 2020) but is much lower than required in interaction-powered SNe IIn ($\dot{M} \gtrsim 10^{-3} M_{\odot} \text{yr}^{-1}$; e.g., Smith 2014, 2017). The luminosity available from CSM interactions is

$$L_{\text{CSM}} \approx \dot{M} v_s^3 v_w^{-1} = 2.1 \left[\frac{\dot{M}}{10^{-4} M_{\odot} \text{yr}^{-1}} \right] \left[\frac{v_s}{10^4 \text{ km s}^{-1}} \right]^3 \left[\frac{30 \text{ km s}^{-1}}{v_w} \right] \times 10^{42} \text{ erg s}^{-1}, \quad (3)$$

which would only be sufficient to power the light curve after ~ 50 d. However, with the relatively low densities at this point, the shock would have difficulty thermalising this energy to produce the observed optical emission and the energy would more likely be radiated as X-rays. Using the photospheric velocity ($\sim 6000 \text{ km s}^{-1}$) rather than the $H\alpha$ velocity ($\sim 10,000 \text{ km s}^{-1}$) would reduce the shock luminosity by another factor of five. Moreover, a light curve powered by interaction with a low-velocity wind (as inferred from flash-ionisation lines; see §5.1) would have produced prominent narrow lines of $\sim 100 \text{ km s}^{-1}$ widths in the later spectra, which are clearly missing.

The early X-ray detections during +11 d to +14 d with a luminosity of $\sim 5 \times 10^{41} \text{ erg s}^{-1}$ and the nondetections thereafter indicate even lower CSM densities if the shock luminosity emerges as X-rays. The detections are, however, substantially more luminous than seen in typical SNe IIP/L ($\sim 10^{38}\text{--}10^{39} \text{ erg s}^{-1}$; e.g., Dwarkadas & Gruszko 2012; Bose et al. 2019). This suggests that the progenitor of ASASSN-18am had a relatively denser CSM than typical red supergiant progenitors of SNe IIP/L. In any case, both the flash-ionised spectrum and the X-ray measurements indicate that the density of the CSM is too low to drive an interaction-powered light curve.

6.4 Inferred large ^{56}Ni mass

As discussed in §6.1 and §6.2, radioactive ^{56}Ni is a key component for either model to fit the light curve, especially during the tail phase. The radiative diffusion model requires a ^{56}Ni mass of $\sim 0.4 M_{\odot}$, while the magnetar spin-down model requires a slightly lower mass of $\sim 0.3 M_{\odot}$. Such masses are about an order of magnitude higher than found in typical SNe IIP/L (the median is a few percent of M_{\odot}), and are also considerably higher than estimates for SNe IIb (Kushnir 2015a; Müller et al. 2017; Anderson 2019). Stripped ccSNe (SNe Ib/c) tend to have higher ^{56}Ni masses than SNe II (Kushnir 2015a; Anderson 2019; Sharon & Kushnir 2020). The ^{56}Ni mass estimates for ASASSN-18am are within the range reported for SNe Ib/c (Kushnir 2015a; Anderson 2019) and are remarkably similar to estimates for SNe Ic-BL, which have some of the highest estimated ^{56}Ni masses among ccSNe.

The nebular-phase spectrum of ASASSN-18am shows strong lines of iron-group elements (as discussed in §5.3) which are not seen in SNe II, but are comparable to those in SNe Ic-BL like SNe 1998bw and 2002ap which have ^{56}Ni mass estimates of $\sim 0.35 M_{\odot}$ (Nakamura et al. 2001) and $\sim 0.1 M_{\odot}$ (Mazzali et al. 2007) (respectively) based on detailed spectroscopic modeling. These strong lines also furnish an independent confirmation that ASASSN-18am has produced a massive amount of ^{56}Ni in the explosion. However, detailed modeling is required to quantify this ^{56}Ni mass using nebular spectra. ASASSN-18am is a partially stripped-envelope SN, as inferred from the presence of helium and the nebular-phase spectra with weak hydrogen. The partially stripped envelope and the high expansion velocity lead to fast rarefaction of the ejecta, consistent with the low γ -ray trapping parameter $t_{0\gamma}$ we estimated from light curve models.

The popular neutrino-driven explosion models are unable to produce M_{Ni} higher than $\sim 0.2 M_{\odot}$ (e.g., Sukhbold et al. 2016; Ertl et al. 2020). This poses a serious challenge for explaining many ccSNe, particularly stripped ccSNe with high M_{Ni} estimates reported in the literature (see e.g., Valenti et al. 2012; Anderson 2019). Sometimes, the magnetar model is invoked to substantially reduce the high ^{56}Ni mass (e.g., Wang et al. 2016). However, this does not work for ASASSN-18am, as the magnetar model only slightly reduced the required M_{Ni} to $0.3 M_{\odot}$, which is still inconsistent with neutrino-driven explosion models. On the other hand, $M_{\text{Ni}} \geq 0.2 M_{\odot}$ may be synthesised by a strong magnetar itself as suggested by Suwa & Tominaga (2015), but our best-fit magnetar parameters for ASASSN-18am do not satisfy their constraint. Another possibility is the collapse-induced thermonuclear explosion models for ccSNe (Kushnir & Katz 2015; Kushnir 2015a,b), which can produce such large ^{56}Ni masses and high kinetic energies (Kushnir 2015b). Pair-instability SN models are also known to produce very large amounts of ^{56}Ni but have extended light curves peaking after several tens of days (Kasen et al. 2011), incompatible with ASASSN-18am.

6.5 Fallback accretion power

Fallback accretion onto a black hole following a neutrino-driven explosion of a massive progenitor may produce light curves with a wide range of luminosities. (e.g., Utrobin et al. 2010; Moriya et al. 2019). In such a model any ^{56}Ni produced in the shock is accreted onto the black hole remnant without contributing to radioactive heating, and accretion power is the only source of energy powering the late-time light curves. Moriya et al. (2019) modeled the explosion of a $40 M_{\odot}$ progenitor and produced a range of light

curves depending on the accretion efficiency and the delay time of the fallback. These models could reproduce the light curves of normal-luminosity SNe II (SN 1987A and SN 1999em), relatively luminous SNe II (OGLE-2014-SN-073, Terreran et al. 2017; SN 2009kf, Botticella et al. 2010), and also SLSN-II (SN 2008es, Miller et al. 2009). The fallback accretion powering mechanism is also a possibility for ASASSN-18am. However, unlike the light curve of ASASSN-18am, these models show a long rise-to-peak time and slow decline rates. Moreover, as a consequence of the fallback, these models predict very low or no ^{56}Ni mass to be present in the ejecta, which contradicts the presence of strong nebular lines of iron-group elements suggesting a high ^{56}Ni mass yield.

7 OXYGEN MASS AND NEBULAR EMISSION

The strength of the [O I] $\lambda\lambda 6300, 6364$ emission line is directly related to the mass of oxygen produced in the core, which in turn depends on the ZAMS mass (e.g., Woosley & Weaver 1995; Thielemann et al. 1996). As previously noted, the +211 d nebular spectrum shows unusually strong [O I] emission as compared to other lines (e.g., Fe II, H I, He I, Ca II). In Figure 15 the [O I] emission profile of ASASSN-18am is compared in luminosity with that of other hydrogen-rich SNe. The [O I] luminosity of ASASSN-18am is brighter than that of SN II 2012aw, SN IIb 1993J, LSN-II ASASSN-15nx, and SN II 2015bs. SN 2015bs is claimed to have had one of the highest mass progenitors for a SN II ($\sim 21 M_{\odot}$; Anderson et al. 2018). SN 2012aw is an archetypal SN IIP having direct identification of the progenitor from *HST* images with a mass of $\sim 18 M_{\odot}$ (Van Dyk et al. 2012; Fraser et al. 2012). This indicates that ASASSN-18am has a high O I mass and consequently a massive progenitor when compared with most SNe II.

However, the temperature and line opacities must also be considered in order to accurately estimate the O I mass. We can estimate the O I mass using the method described by Jerkstrand et al. (2014). This requires an estimate of the O I temperature, which can be done using the line ratios of [O I] $\lambda 5577$ and [O I] $\lambda\lambda 6300, 6364$, as both are collisionally excited but with different temperature dependencies. In our nebular spectrum [O I] $\lambda 5577$ is marginally detected and partially blended with [Fe II] $\lambda 5528$. Using a two-component Gaussian model, we deblend the lines to estimate an [O I] $\lambda 5577$ luminosity of $0.9 \times 10^{38} \text{ erg s}^{-1}$. Since the [O I] $\lambda 5577$ detection is marginal and a higher [O I] $\lambda 5577$ luminosity relative to [O I] $\lambda\lambda 6300, 6364$ leads to a lower estimate of the oxygen mass, we adopted an upper limit to the [O I] $\lambda 5577$ luminosity of $1.5 \times 10^{38} \text{ erg s}^{-1}$, corresponding to the nominal value plus three times the uncertainty estimate, to produce a conservative (i.e., biased low) estimate of the oxygen mass.

Estimating the [O I] $\lambda\lambda 6300, 6364$ flux is nontrivial because of strong and broad emission (possibly a blend of He I, [N II], and H α) on the red wing of the profile. As shown in Figure 16, we use four components to fit the full profile, where two of the components are for the 6300, 6364 Å doublet, and the other two (a narrow and a broad component) are to model the additional blended flux (see more discussion below). We measure a combined [O I] doublet luminosity of $2.8 \times 10^{39} \text{ erg s}^{-1}$. In the optically thick limit, the [O I] $\lambda 6300$ /[O I] $\lambda 6340$ line intensity ratio is ~ 1 , whereas in the optically thin limit the ratio is ~ 3 . From our multicomponent fit we measure the 6300/6364 line ratio to be ~ 1.2 , which implies that the doublet emission is partially transitioning to optical thinness. Therefore, we follow the arguments by Jerkstrand et al. (2014) and adopt Sobolev (1957) escape probabilities of $\beta_{6300,6364} \approx 0.5$

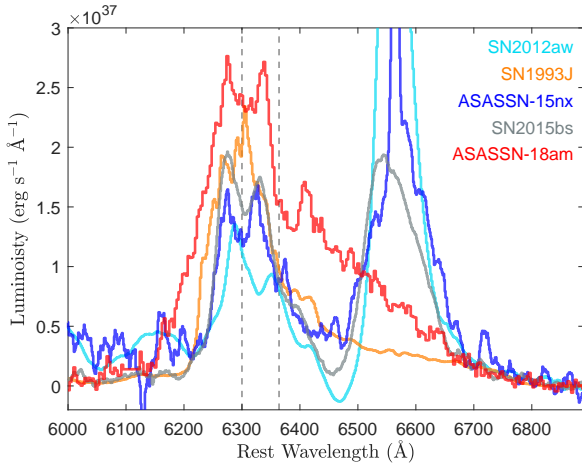


Figure 15. The luminosity of the [O I] emission profile of ASASSN-18am as compared to that of other SNe II. For the comparison sample, the spectroscopic flux is dereddened and is recalibrated using available photometry. All of the spectra have the local continuum subtracted using a line-free region near 6850 Å. The phases and references for the spectra are the same as in Fig. 11.

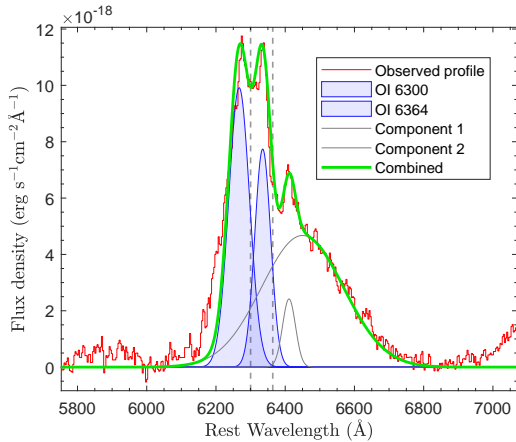


Figure 16. Decomposition of the blended [O I] $\lambda\lambda 6300, 6364$ emission profile in the +211 d nebular-phase spectrum. The spectrum pseudocontinuum has been subtracted, and a reddening correction was applied. The vertical dashed lines show the rest wavelengths of the [O I] doublet.

and $\beta_{5577}/\beta_{6300,6364} \approx 1-2$. From this we estimate that the O I temperature is 3600–4000 K and finally obtain an oxygen mass of $M_{\text{O}} = 1.8-3.4 M_{\odot}$. This is significantly more massive than most normal SNe II/Ib (e.g., SNe 2004et, 2012aw, 1993J, and 2011dh). As shown in Figure 17, the oxygen mass yield varies monotonically with the initial progenitor M_{ZAMS} . Based on these scaling relations, the estimated O I mass implies an initial mass of $M_{\text{ZAMS}} = 19-26 M_{\odot}$ or $M_{\text{ZAMS}} = 22 M_{\odot}$ by assuming a mean β ratio of 1.5. Since most of the oxygen is produced during the hydrostatic burning phase, changes in the explosion physics should have little effect on O I to ZAMS mass-scaling relation. Note that the dominant sources of uncertainties in the O I mass estimates are the measurements of [O I] $\lambda 5577$ and [O I] $\lambda\lambda 6300, 6364$ line fluxes. However, both of these measurements were made such as to ensure that we obtain a conservative estimate of the resulting O I mass. If the extended red wing in the [O I] $\lambda\lambda 6300, 6364$ profile is a blend of multiple emission lines in that region, then we would expect an asymmetric

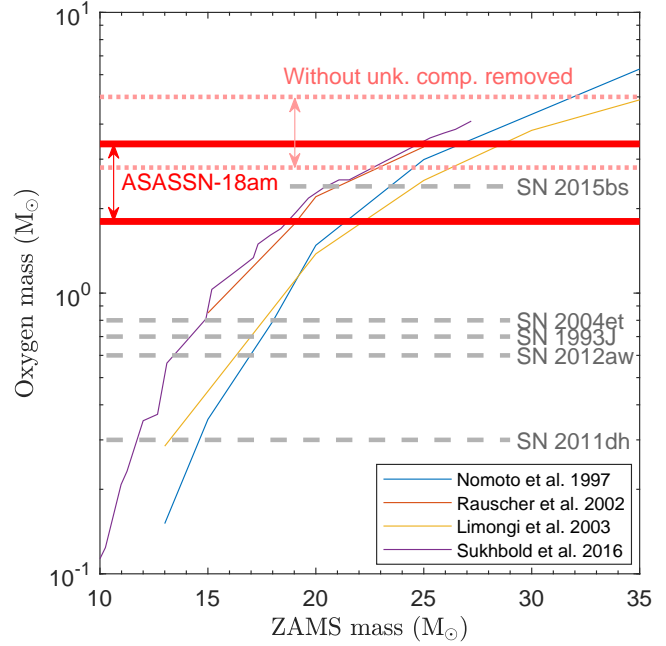


Figure 17. The final oxygen mass as a function of the progenitor ZAMS mass for the models of Nomoto et al. (1997), Rauscher et al. (2002), Limongi & Chieffi (2003), and Sukhbold et al. (2016). The pair of red solid lines shows the range of O I mass estimated for ASASSN-18am. The red dashed lines indicate the increase in the resulting O I mass if we assume there is no contamination of the line (i.e., unknown components not removed; see Fig. 16). For comparison, the O I mass estimates for the normal SNe II 2004et, 2012aw, 1993J, and 2011dh (Jerkstrand et al. 2012, 2014, 2015) are denoted by grey dashed lines. We also estimated the O I mass for SN 2015bs to be $\sim 1.7-3.1 M_{\odot}$ using the spectrum from Anderson et al. (2018), and the implied ZAMS mass is consistent with their estimate.

and red-skewed profile for the unknown broad component (refer to Fig. 16) implying a larger [O I] flux and an optically thick line (i.e., $\beta_{6300,6364} < 0.5$), which will only result in a higher derived O I mass.

We also examined the [O I] $\lambda\lambda 6300, 6364/[\text{Ca II}]\lambda\lambda 7291, 7324$ line intensity ratio. This ratio is sensitive to the core mass and hence to the initial progenitor mass, while being minimally dependent on temperature and density (Fransson & Chevalier 1989; Elmhamdi et al. 2004). In SNe IIP/L the line ratio is typically $\lesssim 0.7$ (Kuncarayakti et al. 2015). For ASASSN-18am, we estimate that the [O I]/[Ca II] line ratio is ~ 2.3 , also implying a significantly higher progenitor mass. To further compare the line ratio with that of various progenitor masses, we use the model spectra from Jerkstrand et al. (2014) for the mass range 12–25 M_{\odot} and extract the [O I]/[Ca II] line ratios. After 250 d past explosion, the ratios are found to be almost constant. The ratio of ~ 2.0 for the highest 25 M_{\odot} model is closest to (albeit slightly lower than) the value we find for ASASSN-18am. For the lower mass models, the line ratio monotonically decreases.

On modeling the [O I] emission in the +211 d spectrum with multicomponent Gaussian profiles (see Fig. 16), we find that the doublet is blueshifted by $\sim 1350 \text{ km s}^{-1}$. A similar blueshift is also seen for the [Ca II] doublet. As mentioned above, for the decomposition of the [O I] profile we used two more components in addition to the [O I] doublet. One is to fit the weak narrow component at $\sim 6408 \text{ \AA}$ (Component-1 of Figure 16) and the other is to fit the ex-

cess flux on the blue wing (Component-2). We could not ascertain the exact origin of these two components, but we speculate these are likely blends of He I, [N II], and also possibly residual H α . Another possibility is that Component-1 (narrow) is a redshifted component of double-peaked [O I] emission. However, from our spectrum we cannot firmly determine any presence of double-peaked structure in the [O I] and [Ca II] profiles, which would otherwise imply a bipolar core geometry. The observed blueshift can be a consequence of asymmetry in the inner ejecta, residual opacity in the core, or possibly the formation of dust (Taubenberger et al. 2009). If Component-1 is associated with [O I] due to bipolar geometry or if the blueshifted emission is a consequence of dust formation, then both of these scenarios would imply an even higher oxygen mass and consequently a higher ZAMS mass.

A progenitor of $M_{\text{ZAMS}} \approx 20\text{--}25 M_{\odot}$ will explode with a helium-core mass of $M_{\text{He}} \approx 6\text{--}8 M_{\odot}$ (Hirschi et al. 2004). Therefore, including the mass of the hydrogen envelope, the progenitor mass at the time of explosion will be $> 6\text{--}8 M_{\odot}$. However, in the radiative diffusion model the estimated ejecta mass is $\lesssim 4 M_{\odot}$ (see §6.1), and the implied mass of the compact remnant will be $> 2\text{--}4 M_{\odot}$. Given the overall systematic uncertainties in mass estimates, the nature of the resulting remnant is uncertain, but a black hole may be favoured.

8 SUMMARY

We presented discovery and follow-up observations of the luminous hydrogen-rich SN ASASSN-18am. The light curve peaked at $M_V \approx -19.7$ mag, which is between that of normal ccSNe and SLSNe. The photospheric phase light curve exhibits a very steep decline of $6.0 \text{ mag } (100 \text{ d})^{-1}$, making it one of the fastest-declining SNe II. The earliest spectrum at +2.4 d shows flash-ionised features of H I and He II, after which the spectra became featureless with only a blue continuum until 18.2 d. ASASSN-18am is the first LSN-II having a spectrum sufficiently early to see the flash-ionisation features and from this we estimated that the star had a CSM wind of $\dot{M} \approx 2 \times 10^{-4} M_{\odot} \text{ yr}^{-1}$. The early X-ray detections imply lower mass-loss rates but the X-rays may be partly thermalised at these phases. The later X-ray nondetections would seem to require lower CSM densities.

By spectroscopic definition ASASSN-18am is a Type IIb SN because of persistent He I lines identified in its spectra. The presence of helium and weak unresolved H α at late phases suggests partially hydrogen-depleted ejecta. Other than these He I lines, ASASSN-18am is both photometrically and spectroscopically different from generic SNe IIb. Its overall energy budget is also significantly higher. In SNe IIb, the Balmer emission lines decay quickly after peak brightness and He I starts to dominate in the 6300–6900 Å region, but ASASSN-18am has stronger Balmer emissions than SNe IIb at coeval epochs. This seems to place ASASSN-18am between generic SNe IIP/L and SNe IIb in terms of the hydrogen content of its ejecta. The expansion velocities measured for H α , H β , and Fe II in ASASSN-18am are unusually high for a SN II. The earliest H α absorption-minimum velocity is $17,000 \text{ km s}^{-1}$, which is never seen in normal SNe II. The nebular-phase spectra showed very strong [O I] $\lambda\lambda 6300, 6364$ emission, suggesting a massive progenitor. Using the [O I] luminosity we estimate the O I core mass to be $\sim 1.7\text{--}3.1 M_{\odot}$ which corresponds to a progenitor mass of $\sim 19\text{--}24 M_{\odot}$. We also found a high [O I]/[Ca II] line ratio of ~ 2.3 , exceeding by a factor of three that of typical SNe IIP/L, which also suggests a massive progenitor.

We investigated a range of possible powering mechanisms for ASASSN-18am. Both the radiative diffusion and magnetar spin-down model support a low-mass envelope with high kinetic energy, which is consistent with our spectroscopic observations. The radiative diffusion model would require a large ^{56}Ni mass of $0.4 M_{\odot}$ and a high γ -ray leakage rate to fit the light curve. The magnetar spin-down model requires slightly lower values for both the nickel mass ($0.3 M_{\odot}$) and γ -ray leakage. The nebular-phase spectrum shows strong lines of iron-group elements, also indicating a high ^{56}Ni mass. Such strong lines are similar to those in many SNe Ic-BL but are never seen in typical SNe II. However, the large ^{56}Ni masses estimated from both models are difficult or impossible to produce in a neutrino-driven explosion. On the other hand, we could not find any evidence to support the CSM interaction scenario. The CSM density, whether derived from the flash-ionisation emission lines or the X-ray luminosities, is too low to produce the observed luminosity through CSM interaction.

ASASSN-18am is the latest addition to the small number of luminous H-rich SNe. In this work we refer to them as LSNe-II. Other examples are PTF10iam (Arcavi et al. 2016), SN 2013fc (Kangas et al. 2016), ASASSN-15nx (Bose et al. 2018), and SN 2016gsd (Reynolds et al. 2020). Although these SNe (see Fig. 3) do not represent a statistically complete sample, however, it likely disproves the existence of a true gap between normal SNe and SLSNe as was previously thought (Arcavi et al. 2016). LSNe-II have peak absolute magnitudes of ~ -20 mag, about 2–3 mag more luminous than typical ccSNe. They all have relatively short rise-to-peak times of ~ 15 d, followed by a rapid decline in light curves. These SNe also have relatively weak H I line profiles compared to SNe IIP/L. SNe with ejecta-CSM interaction (SNe IIn) can be similarly luminous, but the absence of any obvious spectroscopic signature of interaction in LSNe-II distinguish them from the SN IIn population, so their powering mechanism is an open question. In previous examples, CSM models with weak interaction signatures could still be invoked. However, for ASASSN-18am we know that the system lacks a sufficiently dense CSM to account for its high luminosity.

We can update the rate estimate for LSNe-II-like events given by Bose et al. (2018) based on one event (ASASSN-15nx) and the ASAS-SN survey running time of 2.7 yr. Now, with ASASSN-18am, we have two LSNe-II detected in the ASAS-SN survey. Counting through the end of year 2019, ASAS-SN has been running for 5.7 yr. So, we can simply scale up the time-based rate estimate from Bose et al. (2018) by a factor of $2 \times 2.7 / 5.7 \approx 0.95$. Therefore, the updated time-based rate would be $r \approx 27 \text{ Gpc}^{-3} \text{ yr}^{-1}$. An alternative rate estimate given by Bose et al. (2018) was to scale relative to the 499 SNe Ia in ASAS-SN by the end of 2016. ASAS-SN has discovered 528 SNe Ia through the end of 2017 (Holoien et al. 2019), which scales to ~ 700 SNe Ia by the end of 2019. Thus, this second estimate is updated by a factor of $2 \times 449 / 700 \approx 1.28$ to give $r \approx 22 \text{ Gpc}^{-3} \text{ yr}^{-1}$, consistent with the estimated based on survey time. This means that the LSN-II rate is comparable with the SLSN-I rate ($91 \text{ Gpc}^{-3} \text{ yr}^{-1}$; Prajs et al. 2017), which indicates a possible continuity in the luminosity function between normal ccSNe and SLSNe.

ACKNOWLEDGMENTS

An anonymous referee provided helpful suggestions for improving this paper. We thank Boaz Katz and Amir Sharon for their assistance, and Dan Perley for reducing the Keck/LRIS +8.3 d spectrum. K.Z.S. and C.S.K. are supported by NSF grants AST-1515927,

AST-1814440, and AST-1908570. M.S. is supported by a project grant (8021-00170B) from the Independent Research Fund Denmark (IRFD) and by generous grants (13261 and 28021) from VILLUM FONDEN. B.J.S. is supported by NSF grants AST-1907570, AST-1908952, AST-1920392, and AST-1911074. Support for J.L.P. is provided in part by FONDECYT through grant 1191038 and by the Ministry of Economy, Development, and Tourism's Millennium Science Initiative through grant IC120009, awarded to The Millennium Institute of Astrophysics, MAS. T.A.T. is supported in part by NASA grant 80NSSC20K0531. K.A.A. is supported by the Danish National Research Foundation (DNRF132). Parts of this research were supported by the Australian Research Council Centre of Excellence for All Sky Astrophysics in 3 Dimensions (ASTRO 3D), through project number CE170100013. J.Z. is supported by the National Natural Science Foundation of China (grants 11803049, 41727803). A.V.F.'s supernova group is grateful for financial assistance from the Christopher R. Redlich Fund, the TABASGO Foundation, and the Miller Institute for Basic Research in Science (U.C. Berkeley).

ASAS-SN is supported by the Gordon and Betty Moore Foundation through grant GBMF5490 to the Ohio State University, and by NSF grants AST-1515927 and AST-1908570. Development of ASAS-SN was supported by NSF grant AST-0908816, the Mt. Cuba Astronomical Foundation, the Center for Cosmology and AstroParticle Physics at the Ohio State University, the Chinese Academy of Sciences South America Center for Astronomy (CASSACA), the Villum Foundation, and George Skestos. Some of the data presented herein were obtained at the W. M. Keck Observatory, which is operated as a scientific partnership among the California Institute of Technology, the University of California, and NASA; the Observatory was made possible by the generous financial support of the W. M. Keck Foundation. We thank the staffs at Lick and Keck Observatories for their assistance. Research at Lick Observatory is partially supported by a generous gift from Google.

We acknowledge the support of the staff of the Xinglong 2.16 m telescope. This work was partially supported by the Open Project Program of the CAS Key Laboratory of Optical Astronomy, National Astronomical Observatories, Chinese Academy of Sciences. We acknowledge the Telescope Access Program (TAP) funded by NAOC, CAS, and the Special Fund for Astronomy from the Ministry of Finance. This work is partly based on NUTS2 observations made with the NOT, operated by the NOT Scientific Association at the Observatorio del Roque de los Muchachos, La Palma, Spain, of IAC. ALFOSC is provided by IAA under a joint agreement with the University of Copenhagen and NOTSA. NUTS2 is funded in part by the Instrument Center for Danish Astrophysics (IDA). This work is partly based on observations made with the Gran Telescopio Canarias (GTC), installed at the Spanish Observatorio del Roque de los Muchachos of the Instituto de Astrofísica de Canarias, on the island of La Palma.

The LBT is an international collaboration among institutions in the United States, Italy, and Germany. LBT Corporation partners are The University of Arizona on behalf of the Arizona university system; Istituto Nazionale di Astrofisica, Italy; LBT Beteiligungsgesellschaft, Germany, representing the Max-Planck Society, the Astrophysical Institute Potsdam, and Heidelberg University; The Ohio State University; and The Research Corporation, on behalf of The University of Notre Dame, University of Minnesota, and University of Virginia.

DATA AVAILABILITY

The data underlying this article are available in the article and in its online supplementary material.

REFERENCES

- Anderson J. P., 2019, *A&A*, 628, A7
 Anderson J. P. et al., 2014, *ApJ*, 786, 67
 Anderson J. P. et al., 2018, *Nature Astronomy*, 2, 574
 Arcavi I. et al., 2016, *ApJ*, 819, 35
 Arnett W. D., 1980, *ApJ*, 237, 541
 Arnett W. D., Fu A., 1989, *ApJ*, 340, 396
 Barbon R., Ciatti F., Rosino L., 1979, *A&A*, 72, 287
 Barbon R., Ciatti F., Rosino L., 1982a, *A&A*, 116, 35
 Barbon R., Ciatti F., Rosino L., Ortolani S., Rafanelli P., 1982b, *A&A*, 116, 43
 Barkat Z., Rakavy G., Sack N., 1967, *Phys. Rev. Lett.*, 18, 379
 Beasor E. R., Davies B., Smith N., van Loon J. T., Gehrz R. D., Figer D. F., 2020, *MNRAS*, 492, 5994
 Benetti S. et al., 2018, *MNRAS*, 476, 261
 Bose S., Kumar B., 2014, *ApJ*, 782, 98
 Bose S. et al., 2013, *MNRAS*, 433, 1871
 Bose S. et al., 2015a, *MNRAS*, 450, 2373
 Bose S. et al., 2015b, *ApJ*, 806, 160
 Bose S., Kumar B., Misra K., Matsumoto K., Kumar B., Singh M., Fukushima D., Kawabata M., 2016, *MNRAS*, 455, 2712
 Bose S. et al., 2018, *ApJ*, 862, 107
 Bose S. et al., 2019, *ApJL*, 873, L3
 Botticella M. T. et al., 2010, *ApJL*, 717, L52
 Bouchet P., Danziger I. J., 1993, *A&A*, 273, 451
 Branch D. et al., 2002, *ApJ*, 566, 1005
 Breeveld A. A., Landsman W., Holland S. T., Roming P., Kuin N. P. M., Page M. J., 2011, in J.E. McEnery, J.L. Racusin, N. Gehrels, eds, *American Institute of Physics Conference Series*. American Institute of Physics Conference Series, Vol. 1358, pp. 373–376
 Brinacombe J., Stone G., Stanek K. Z., 2018, *Transient Name Server Discovery Report*, 2018-54, 1
 Brinchmann J., Charlot S., White S. D. M., Tremonti C., Kauffmann G., Heckman T., Brinkmann J., 2004, *MNRAS*, 351, 1151
 Brown T. M. et al., 2013, *PASP*, 125, 1031
 Burbidge E. M., Burbidge G. R., Fowler W. A., Hoyle F., 1957, *Reviews of Modern Physics*, 29, 547
 Burrows D. N. et al., 2005, *Space Sci. Rev.*, 120, 165
 Childress M. J. et al., 2015, *MNRAS*, 454, 3816
 Chugai N. N., 2007, in S. Immler, K. Weiler, R. McCray, eds, *Supernova 1987A: 20 Years After: Supernovae and Gamma-Ray Bursters*. American Institute of Physics Conference Series, Vol. 937, pp. 357–364
 Chugai N. N., 2009, *MNRAS*, 400, 866
 Chugai N. N., 2019, *Astronomy Letters*, 45, 427
 de Jager C., Nieuwenhuijzen H., van der Hucht K. A., 1988, *A&AS*, 72, 259
 de Vaucouleurs G., de Vaucouleurs A., Buta R., Ables H. D., Hewitt A. V., 1981, *PASP*, 93, 36
 Dessart L., Audit E., 2018, *A&A*, 613, A5
 Doggett J. B., Branch D., 1985, *AJ*, 90, 2303
 Dwarkadas V. V., Gruszko J., 2012, *MNRAS*, 419, 1515
 Elmhamdi A., Danziger I. J., Cappellaro E., Della Valle M., Guiffes C., Phillips M. M., Turatto M., 2004, *A&A*, 426, 963

- Elmhamdi A. et al., 2003, MNRAS, 338, 939
- Ergon M. et al., 2015, A&A, 580, A142
- Ertl T., Woosley S. E., Sukhbold T., Janka H. T., 2020, ApJ, 890, 51
- Fabricant D., Cheimets P., Caldwell N., Geary J., 1998, PASP, 110, 79
- Faran T. et al., 2014, MNRAS, 445, 554
- Filippenko A. V., 1982, PASP, 94, 715
- Filippenko A. V., 1988, AJ, 96, 1941
- Filippenko A. V., 1997, ARA&A, 35, 309
- Filippenko A. V., Matheson T., Ho L. C., 1993, ApJL, 415, L103
- Fisher A., Branch D., Nugent P., Baron E., 1997, ApJL, 481, L89
- Foley R. J. et al., 2003, PASP, 115, 1220
- Fowler W. A., Hoyle F., 1964, ApJS, 9, 201
- Fransson C., Chevalier R. A., 1989, ApJ, 343, 323
- Fransson C. et al., 2014, ApJ, 797, 118
- Fraser M. et al., 2012, ApJL, 759, L13
- Gal-Yam A., 2019, ARA&A, 57, 305
- Gal-Yam A. et al., 2014, Nature, 509, 471
- Gehrels N. et al., 2004, ApJ, 611, 1005
- Gompertz B. P., O'Brien P. T., Wynn G. A., Rowlinson A., 2013, MNRAS, 431, 1745
- Gutiérrez C. P. et al., 2017, ApJ, 850, 89
- Hamuy M., Suntzeff N. B., 1990, AJ, 99, 1146
- Henden A. A., Templeton M., Terrell D., Smith T. C., Levine S., Welch D., 2016, VizieR Online Data Catalog, 2336
- Hirschi R., Meynet G., Maeder A., 2004, A&A, 425, 649
- Holoien T. W. S. et al., 2019, MNRAS, 484, 1899
- Hoyle F., Fowler W. A., 1960, ApJ, 132, 565
- Insera C. et al., 2012, MNRAS, 422, 1122
- Jeffery D. J., 1999, ArXiv Astrophysics e-prints, astro-ph/9907015
- Jerkstrand A., Fransson C., Maguire K., Smartt S., Ergon M., Spyromilio J., 2012, A&A, 546, A28
- Jerkstrand A., Smartt S. J., Fraser M., Fransson C., Sollerman J., Taddia F., Kotak R., 2014, MNRAS, 439, 3694
- Jerkstrand A., Ergon M., Smartt S. J., Fransson C., Sollerman J., Taubenberger S., Bersten M., Spyromilio J., 2015, A&A, 573, A12
- Kalberla P. M. W., Burton W. B., Hartmann D., Arnal E. M., Bajaja E., Morras R., Pöppel W. G. L., 2005, A&A, 440, 775
- Kangas T. et al., 2016, MNRAS, 456, 323
- Kasen D., Bildsten L., 2010, ApJ, 717, 245
- Kasen D., Woosley S. E., Heger A., 2011, ApJ, 734, 102
- Katz B., Kushnir D., Dong S., 2013, ArXiv e-prints, arXiv:1301.6766
- Kelly P. L., Kirshner R. P., 2012, ApJ, 759, 107
- Khazov D. et al., 2016, ApJ, 818, 3
- Kochanek C. S., 2019, MNRAS, 483, 3762
- Kochanek C. S. et al., 2017, PASP, 129, 104502
- Kotak R. et al., 2009, ApJ, 704, 306
- Kriek M., van Dokkum P. G., Labbé I., Franx M., Illingworth G. D., Marchesini D., Quadri R. F., 2009, ApJ, 700, 221
- Kuncarayakti H. et al., 2015, A&A, 579, A95
- Kushnir D., 2015a, ArXiv e-prints, 1506.02655
- Kushnir D., 2015b, ArXiv e-prints, 1502.03111
- Kushnir D., Katz B., 2015, ApJ, 811, 97
- Lee G. H., Hwang H. S., Lee M. G., Ko J., Sohn J., Shim H., Diaferio A., 2015, ApJ, 800, 80
- Leonard D. C. et al., 2002, PASP, 114, 35
- Limongi M., Chieffi A., 2003, ApJ, 592, 404
- Maguire K. et al., 2010, MNRAS, 404, 981
- Martini P. et al., 2011, PASP, 123, 187
- Massey P., Gronwall C., 1990, ApJ, 358, 344
- Mattila S. et al., 2008, MNRAS, 389, 141
- Mazzali P. A. et al., 2007, ApJ, 670, 592
- Meikle W. P. S. et al., 2011, ApJ, 732, 109
- Metzger B. D., Thompson T. A., Quataert E., 2007, ApJ, 659, 561
- Miller A. A. et al., 2009, ApJ, 690, 1303
- Moriya T. J., Müller B., Chan C., Heger A., Blinnikov S. I., 2019, ApJ, 880, 21
- Müller T., Prieto J. L., Pejcha O., Clocchiatti A., 2017, ApJ, 841, 127
- Nagy A. P., Vinkó J., 2016, A&A, 589, A53
- Nakamura T., Mazzali P. A., Nomoto K., Iwamoto K., 2001, ApJ, 550, 991
- Nakar E., Poznanski D., Katz B., 2016, ApJ, 823, 127
- Nicholl M., Guillochon J., Berger E., 2017, ApJ, 850, 55
- Niemela V. S., Ruiz M. T., Phillips M. M., 1985, ApJ, 289, 52
- Nomoto K., Hashimoto M., Tsujimoto T., Thielemann F. K., Kishimoto N., Kubo Y., Nakasato N., 1997, Nucl. Phys. A, 616, 79
- Oke J. B. et al., 1995, PASP, 107, 375
- Pastorello A. et al., 2006, MNRAS, 370, 1752
- Pastorello A. et al., 2008, MNRAS, 389, 113
- Pastorello A. et al., 2009, MNRAS, 394, 2266
- Patat F. et al., 2001, ApJ, 555, 900
- Perley D. A., 2019, PASP, 131, 084503
- Planck Collaboration et al., 2016, A&A, 594, A13
- Pogge R. W. et al., 2010, in Proc. SPIE. Society of Photo-Optical Instrumentation Engineers (SPIE) Conference Series, Vol. 7735, p. 77350A
- Prajs S. et al., 2017, MNRAS, 464, 3568
- Pun C. S. J. et al., 1995, ApJS, 99, 223
- Quimby R. M., Aldering G., Wheeler J. C., Höflich P., Akerlof C. W., Rykoff E. S., 2007, ApJL, 668, L99
- Quimby R. M. et al., 2011, Nature, 474, 487
- Rauscher T., Heger A., Hoffman R. D., Woosley S. E., 2002, ApJ, 576, 323
- Reynolds T. M. et al., 2020, MNRAS, 493, 1761
- Richmond M. W., Treffers R. R., Filippenko A. V., Paik Y., 1996, AJ, 112, 732
- Sahu D. K., Anupama G. C., Sridvidya S., Muneer S., 2006, MNRAS, 372, 1315
- Sanders N. E. et al., 2015, ApJ, 799, 208
- Schlaflly E. F., Finkbeiner D. P., 2011, ApJ, 737, 103
- Schlegel E. M., 1990, MNRAS, 244, 269
- SDSS Collaboration et al., 2017, ApJS, 233, 25
- Shappee B. J. et al., 2014, ApJ, 788, 48
- Sharon A., Kushnir D., 2020, arXiv e-prints, arXiv:2004.07244
- Skrutskie M. F. et al., 2006, AJ, 131, 1163
- Smith N., 2014, ARA&A, 52, 487
- Smith N., 2017, Interacting Supernovae: Types II_n and Ib_n. p. 403
- Smith N., Mauerhan J. C., Silverman J. M., Ganeshalingam M., Filippenko A. V., Cenko S. B., Clubb K. I., Kandrashoff M. T., 2012, MNRAS, 426, 1905
- Sobacchi E., Granot J., Bromberg O., Sormani M. C., 2017, MNRAS, 472, 616
- Sobolev V. V., 1957, Soviet Ast., 1, 678
- Sukhbold T., Ertl T., Woosley S. E., Brown J. M., Janka H. T., 2016, ApJ, 821, 38
- Suwa Y., Tominaga N., 2015, MNRAS, 451, 282
- Takáts K., Vinkó J., 2006, MNRAS, 372, 1735
- Taubenberger S. et al., 2009, MNRAS, 397, 677
- Terreran G. et al., 2016, MNRAS, 462, 137
- Terreran G. et al., 2017, Nature Astronomy, 1, 713

- Thielemann F. K., Nomoto K., Hashimoto M. A., 1996, *ApJ*, 460, 408
- Thompson T. A., Chang P., Quataert E., 2004, *ApJ*, 611, 380
- Tomasella L. et al., 2013, *MNRAS*, 434, 1636
- Tremonti C. A. et al., 2004, *ApJ*, 613, 898
- Utrobin V. P., Chugai N. N., Botticella M. T., 2010, *ApJL*, 723, L89
- Valenti S. et al., 2012, *ApJL*, 749, L28
- Valenti S. et al., 2014, *MNRAS*, 438, L101
- Valenti S. et al., 2015, *MNRAS*, 448, 2608
- Van Dyk S. D. et al., 2012, *ApJ*, 756, 131
- Villanueva S., Eastman J. D., Gaudi B. S., Pogge R. W., Stassun K. G., Trueblood M., Trueblood P., 2016, *DEDicated MONitor of EXotransits and Transients (DEMONEXT): a low-cost robotic and automated telescope for followup of exoplanetary transits and other transient events*, Society of Photo-Optical Instrumentation Engineers (SPIE) Conference Series, Vol. 9906. p. 99062L
- Villanueva S., Gaudi B. S., Pogge R., Stassun K. G., Eastman J., Trueblood M., Trueblood P., 2018, in *American Astronomical Society Meeting Abstracts #231*. American Astronomical Society Meeting Abstracts, Vol. 231, p. 314.02
- Wang L. J., Han Y. H., Xu D., Wang S. Q., Dai Z. G., Wu X. F., Wei J. Y., 2016, *ApJ*, 831, 41
- Woosley S. E., Weaver T. A., 1995, *ApJS*, 101, 181
- Yoshii Y. et al., 2003, *ApJ*, 592, 467
- Yuan F. et al., 2016, *MNRAS*, 461, 2003

Table 1: Optical photometry of ASASSN-18am in *BVgriz* bands.

UT Date (yyyy-mm-dd)	JD 2458000+	Phase ^a (day)	<i>B</i> (mag)	<i>V</i> (mag)	<i>g</i> (mag)	<i>r</i> (mag)	<i>i</i> (mag)	<i>z</i> (mag)	Tel ^b /Inst
2018-01-10.66	129.16	-1.4	—	non-detection <17.8	—	—	—	—	ASASSN
2018-01-11.66	130.16	-0.4	—	non-detection <17.6	—	—	—	—	ASASSN
2018-01-12.50	131.00	0.4	—	—	16.834 ± 0.086	—	—	—	ASASSN
2018-01-13.65	132.15	1.5	—	16.777 ± 0.126	—	—	—	—	ASASSN
2018-01-14.60	133.10	2.4	—	16.832 ± 0.116	16.471 ± 0.064	—	—	—	ASASSN
2018-01-15.56	134.06	3.4	—	16.554 ± 0.096	16.363 ± 0.064	—	—	—	ASASSN
2018-01-17.47	135.97	5.2	—	16.428 ± 0.254	—	16.325 ± 0.124	—	—	DN
2018-01-17.51	136.01	5.2	16.296 ± 0.042	16.405 ± 0.027	—	16.452 ± 0.021	16.643 ± 0.019	—	PO
2018-01-17.63	136.13	5.4	—	16.363 ± 0.077	—	—	—	—	ASASSN
2018-01-18.47	136.97	6.2	16.244 ± 0.037	16.373 ± 0.051	—	16.362 ± 0.041	16.502 ± 0.060	—	DN
2018-01-18.55	137.05	6.3	—	16.247 ± 0.042	16.227 ± 0.027	16.407 ± 0.026	16.508 ± 0.043	—	Iowa
2018-01-19.49	137.99	7.2	16.103 ± 0.014	16.256 ± 0.017	—	16.315 ± 0.018	16.445 ± 0.023	—	LCOGT
2018-01-19.49	137.99	7.2	16.309 ± 0.072	16.308 ± 0.069	—	16.380 ± 0.086	16.499 ± 0.069	—	DN
2018-01-19.50	138.00	7.2	—	—	16.247 ± 0.050	—	—	—	ASASSN
2018-01-19.55	138.05	7.2	—	16.189 ± 0.045	16.167 ± 0.043	16.354 ± 0.037	16.445 ± 0.052	—	Iowa
2018-01-20.46	138.96	8.1	16.229 ± 0.040	16.158 ± 0.053	—	16.299 ± 0.043	16.500 ± 0.048	—	DN
2018-01-20.51	139.01	8.2	16.158 ± 0.038	16.205 ± 0.026	—	16.227 ± 0.018	16.352 ± 0.014	—	PO
2018-01-20.56	139.06	8.2	—	16.045 ± 0.032	16.117 ± 0.033	16.250 ± 0.025	16.307 ± 0.039	—	Iowa
2018-01-20.56	139.06	8.2	—	16.164 ± 0.069	16.153 ± 0.049	—	—	—	ASASSN
2018-01-21.46	139.96	9.1	16.019 ± 0.017	16.133 ± 0.018	—	16.195 ± 0.015	16.272 ± 0.024	—	LCOGT
2018-01-22.55	141.05	10.1	16.090 ± 0.040	16.136 ± 0.029	—	16.169 ± 0.050	16.286 ± 0.043	—	PO
2018-01-22.56	141.06	10.1	—	16.042 ± 0.036	16.094 ± 0.032	16.167 ± 0.026	16.321 ± 0.038	—	Iowa
2018-01-23.55	142.05	11.1	—	16.059 ± 0.042	16.064 ± 0.025	16.167 ± 0.024	16.204 ± 0.035	—	Iowa
2018-01-24.55	143.05	12.1	16.083 ± 0.042	16.101 ± 0.028	—	16.136 ± 0.031	16.215 ± 0.032	—	PO
2018-01-25.46	143.96	13.0	16.185 ± 0.036	16.083 ± 0.037	—	16.105 ± 0.033	16.249 ± 0.055	—	DN
2018-01-25.55	144.05	13.0	—	16.056 ± 0.042	16.082 ± 0.024	16.175 ± 0.022	16.159 ± 0.038	—	Iowa
2018-01-26.55	145.05	14.0	16.132 ± 0.039	16.105 ± 0.027	—	16.133 ± 0.029	16.192 ± 0.037	—	PO
2018-01-26.55	145.05	14.0	—	16.071 ± 0.047	16.087 ± 0.028	16.135 ± 0.028	—	—	Iowa
2018-01-27.51	146.01	14.9	16.163 ± 0.029	—	16.115 ± 0.052	—	—	—	ASASSN, DN
2018-01-28.46	146.96	15.9	—	—	16.244 ± 0.055	—	—	—	ASASSN
2018-01-28.55	147.05	16.0	—	16.121 ± 0.033	16.160 ± 0.029	16.146 ± 0.022	16.215 ± 0.028	—	Iowa
2018-01-28.56	147.06	16.0	16.142 ± 0.044	16.163 ± 0.036	—	16.158 ± 0.023	16.215 ± 0.013	—	PO
2018-01-29.46	147.96	16.8	16.189 ± 0.021	16.216 ± 0.018	—	16.224 ± 0.016	16.283 ± 0.021	—	LCOGT
2018-01-29.54	148.04	16.9	16.263 ± 0.033	—	—	—	—	—	DN
2018-01-29.55	148.05	16.9	—	16.134 ± 0.046	16.135 ± 0.029	16.198 ± 0.031	16.146 ± 0.043	—	Iowa
2018-01-29.61	148.11	17.0	—	16.257 ± 0.116	—	—	—	—	ASASSN
2018-01-30.46	148.96	17.8	16.344 ± 0.034	16.182 ± 0.036	—	16.252 ± 0.030	16.270 ± 0.032	—	DN
2018-01-30.51	149.01	17.9	16.334 ± 0.040	16.203 ± 0.030	—	16.171 ± 0.020	16.158 ± 0.018	—	PO
2018-01-30.55	149.05	17.9	—	16.132 ± 0.038	16.265 ± 0.029	16.252 ± 0.021	16.219 ± 0.028	—	Iowa
2018-01-30.61	149.11	18.0	—	16.145 ± 0.112	—	—	—	—	ASASSN
2018-01-31.43	149.93	18.7	16.438 ± 0.039	16.294 ± 0.032	—	16.345 ± 0.034	16.348 ± 0.030	—	DN
2018-01-31.55	150.05	18.9	—	16.232 ± 0.045	16.291 ± 0.031	16.238 ± 0.028	16.253 ± 0.036	—	Iowa
2018-01-31.56	150.06	18.9	16.402 ± 0.043	16.278 ± 0.029	—	16.248 ± 0.020	16.304 ± 0.022	—	PO
2018-02-02.45	151.95	20.7	16.566 ± 0.082	16.372 ± 0.104	—	16.413 ± 0.093	16.373 ± 0.127	—	DN
2018-02-02.51	152.01	20.8	16.506 ± 0.045	16.385 ± 0.030	—	16.318 ± 0.021	16.234 ± 0.024	—	PO
2018-02-04.50	154.00	22.7	16.657 ± 0.039	16.465 ± 0.051	—	16.467 ± 0.041	16.407 ± 0.058	—	DN
2018-02-04.51	154.01	22.7	16.645 ± 0.037	16.478 ± 0.027	—	16.415 ± 0.016	16.428 ± 0.020	—	PO
2018-02-05.47	154.97	23.6	—	—	16.528 ± 0.087	—	—	—	ASASSN
2018-02-06.42	155.92	24.6	16.839 ± 0.046	16.589 ± 0.037	—	16.584 ± 0.033	16.522 ± 0.052	—	DN
2018-02-06.44	155.94	24.6	—	—	16.506 ± 0.084	—	—	—	ASASSN
2018-02-06.51	156.01	24.6	16.751 ± 0.037	16.578 ± 0.027	—	16.527 ± 0.023	16.497 ± 0.025	—	PO
2018-02-08.48	157.98	26.6	—	—	16.730 ± 0.081	—	—	—	ASASSN
2018-02-08.51	158.01	26.6	16.853 ± 0.038	16.660 ± 0.026	—	—	—	—	PO
2018-02-08.53	158.03	26.6	—	16.574 ± 0.029	16.705 ± 0.018	16.617 ± 0.020	16.548 ± 0.029	—	Iowa
2018-02-09.49	158.99	27.5	16.909 ± 0.046	16.690 ± 0.051	—	16.603 ± 0.054	16.687 ± 0.035	—	DN
2018-02-09.50	159.00	27.5	16.875 ± 0.019	16.733 ± 0.016	—	16.685 ± 0.014	16.636 ± 0.018	—	LCOGT
2018-02-09.50	159.00	27.5	—	—	16.691 ± 0.074	—	—	—	ASASSN
2018-02-09.54	159.04	27.6	—	16.635 ± 0.027	16.780 ± 0.019	16.662 ± 0.023	16.605 ± 0.033	—	Iowa
2018-02-10.40	159.90	28.4	16.969 ± 0.054	16.774 ± 0.055	—	16.666 ± 0.058	16.643 ± 0.038	—	DN
2018-02-10.44	159.94	28.5	—	—	16.862 ± 0.074	—	—	—	ASASSN
2018-02-10.49	159.99	28.5	17.008 ± 0.044	16.806 ± 0.029	—	16.679 ± 0.036	16.669 ± 0.061	—	PO
2018-02-10.55	160.05	28.6	—	16.678 ± 0.076	—	—	—	—	Iowa
2018-02-11.55	161.05	29.5	—	16.708 ± 0.027	—	—	—	—	Iowa
2018-02-12.40	161.90	30.4	17.204 ± 0.045	16.823 ± 0.029	—	16.805 ± 0.023	16.805 ± 0.043	—	DN
2018-02-12.54	162.04	30.5	—	16.713 ± 0.042	16.918 ± 0.023	16.763 ± 0.020	16.663 ± 0.031	—	Iowa
2018-02-13.39	162.89	31.3	17.223 ± 0.096	16.921 ± 0.055	—	16.927 ± 0.044	16.867 ± 0.055	—	DN
2018-02-13.43	162.93	31.4	17.222 ± 0.046	16.993 ± 0.036	—	16.827 ± 0.071	16.796 ± 0.060	—	LCOGT
2018-02-13.49	162.99	31.4	17.181 ± 0.039	16.935 ± 0.027	—	16.804 ± 0.022	16.807 ± 0.022	—	PO
2018-02-13.54	163.04	31.5	—	16.845 ± 0.027	17.002 ± 0.021	16.823 ± 0.021	16.738 ± 0.035	—	Iowa
2018-02-15.44	164.94	33.3	17.311 ± 0.034	17.060 ± 0.038	—	16.962 ± 0.038	16.964 ± 0.058	—	LCOGT
2018-02-17.52	167.02	35.3	17.460 ± 0.047	17.150 ± 0.046	—	16.991 ± 0.100	17.043 ± 0.103	—	LCOGT
2018-02-17.55	167.05	35.4	17.484 ± 0.044	17.162 ± 0.033	—	17.010 ± 0.028	16.967 ± 0.042	—	PO
2018-02-21.52	171.02	39.2	—	17.381 ± 0.038	17.752 ± 0.071	17.328 ± 0.040	17.055 ± 0.132	—	Iowa

Table 1 - continued.

UT Date (yyyy-mm-dd)	JD 2458000+	Phase ^a (day)	<i>B</i> (mag)	<i>V</i> (mag)	<i>g</i> (mag)	<i>r</i> (mag)	<i>i</i> (mag)	<i>z</i> (mag)	Tel ^b /Inst
2018-02-22.41	171.91	40.1	17.824 ± 0.033	17.458 ± 0.028	—	17.224 ± 0.019	17.172 ± 0.030	—	LCOGT
2018-02-22.54	172.04	40.2	—	17.356 ± 0.036	17.642 ± 0.027	17.224 ± 0.028	17.138 ± 0.040	—	Iowa
2018-02-23.37	172.87	41.0	—	17.430 ± 0.088	—	17.340 ± 0.084	17.254 ± 0.079	—	DN
2018-02-23.49	172.99	41.1	18.007 ± 0.050	17.520 ± 0.028	—	17.277 ± 0.022	17.255 ± 0.016	—	PO
2018-02-25.39	174.89	43.0	18.161 ± 0.059	17.580 ± 0.036	—	17.327 ± 0.028	17.279 ± 0.038	—	LCOGT
2018-02-25.50	175.00	43.1	18.232 ± 0.113	17.511 ± 0.086	—	17.407 ± 0.084	17.472 ± 0.117	—	DN
2018-02-26.36	175.86	43.9	18.279 ± 0.086	17.647 ± 0.059	—	17.470 ± 0.045	17.446 ± 0.084	—	DN
2018-02-27.47	176.97	45.0	18.289 ± 0.073	17.819 ± 0.079	—	17.607 ± 0.052	17.469 ± 0.062	—	DN
2018-02-27.49	176.99	45.0	18.303 ± 0.043	17.775 ± 0.028	—	17.469 ± 0.024	17.442 ± 0.016	—	PO
2018-02-27.53	177.03	45.0	—	17.557 ± 0.051	17.891 ± 0.039	17.351 ± 0.025	—	—	Iowa
2018-03-02.41	179.91	47.8	18.683 ± 0.181	17.990 ± 0.104	—	17.724 ± 0.064	17.597 ± 0.091	—	DN
2018-03-02.53	180.03	47.9	—	18.034 ± 0.066	18.263 ± 0.067	17.662 ± 0.038	—	—	Iowa
2018-03-03.35	180.85	48.7	18.725 ± 0.151	18.036 ± 0.092	—	17.784 ± 0.069	17.634 ± 0.093	—	DN
2018-03-03.47	180.97	48.9	—	18.000 ± 0.085	18.296 ± 0.054	17.745 ± 0.038	—	—	Iowa
2018-03-04.44	181.94	49.8	18.599 ± 0.177	18.156 ± 0.065	18.387 ± 0.037	17.757 ± 0.032	17.703 ± 0.162	—	DN,Iowa
2018-03-05.47	182.97	50.8	—	18.240 ± 0.255	—	17.824 ± 0.176	—	—	Iowa
2018-03-05.49	182.99	50.8	—	18.094 ± 0.053	—	17.770 ± 0.033	17.725 ± 0.040	—	PO
2018-03-06.35	183.85	51.6	18.872 ± 0.152	18.124 ± 0.126	—	17.884 ± 0.148	17.806 ± 0.209	—	DN
2018-03-06.47	183.97	51.8	—	18.180 ± 0.116	18.646 ± 0.097	—	—	—	Iowa
2018-03-07.49	184.99	52.8	18.971 ± 0.058	18.390 ± 0.034	—	17.923 ± 0.025	—	—	PO
2018-03-07.49	184.99	52.8	18.948 ± 0.089	18.324 ± 0.049	—	17.953 ± 0.064	17.793 ± 0.058	—	DN
2018-03-07.53	185.03	52.8	—	18.227 ± 0.055	18.577 ± 0.053	17.885 ± 0.037	—	—	Iowa
2018-03-10.33	187.83	55.5	19.309 ± 0.094	18.542 ± 0.036	—	18.115 ± 0.028	17.975 ± 0.038	—	DN
2018-03-12.52	190.02	57.6	—	18.438 ± 0.090	18.786 ± 0.169	18.191 ± 0.090	—	—	Iowa
2018-03-13.42	190.92	58.5	19.347 ± 0.051	18.656 ± 0.033	18.928 ± 0.121	18.270 ± 0.048	18.141 ± 0.062	—	DN,Iowa
2018-03-14.32	191.82	59.4	19.335 ± 0.106	18.599 ± 0.067	—	18.314 ± 0.063	18.199 ± 0.063	—	DN
2018-03-14.47	191.97	59.5	19.503 ± 0.076	18.685 ± 0.037	—	18.241 ± 0.030	18.110 ± 0.037	—	PO
2018-03-14.52	192.02	59.6	—	18.756 ± 0.068	19.091 ± 0.076	18.179 ± 0.044	—	—	Iowa
2018-03-15.32	192.82	60.3	19.397 ± 0.085	18.676 ± 0.040	—	18.350 ± 0.041	18.236 ± 0.042	—	DN
2018-03-15.43	192.93	60.5	—	18.727 ± 0.054	19.075 ± 0.055	18.236 ± 0.047	—	—	Iowa
2018-03-16.47	193.97	61.5	19.552 ± 0.052	18.779 ± 0.039	—	18.327 ± 0.036	18.315 ± 0.037	—	PO
2018-03-16.51	194.01	61.5	—	18.548 ± 0.089	19.215 ± 0.104	18.257 ± 0.068	—	—	Iowa
2018-03-18.43	195.93	63.4	—	18.835 ± 0.053	19.102 ± 0.031	18.295 ± 0.033	—	—	Iowa
2018-03-20.23	197.73	65.1	19.822 ± 0.064	19.042 ± 0.038	19.367 ± 0.044	18.547 ± 0.028	18.467 ± 0.022	18.301 ± 0.032	LT
2018-03-20.48	197.98	65.4	—	18.944 ± 0.037	—	—	—	—	PO
2018-03-21.49	198.99	66.3	—	18.938 ± 0.042	19.408 ± 0.030	18.480 ± 0.058	—	—	Iowa
2018-03-22.48	199.98	67.3	19.759 ± 0.069	—	—	—	—	—	PO
2018-03-23.34	200.84	68.1	19.956 ± 0.102	19.052 ± 0.069	—	18.600 ± 0.034	18.607 ± 0.046	—	LCOGT
2018-03-24.48	201.98	69.2	—	—	—	18.568 ± 0.032	—	—	PO
2018-03-24.48	201.98	69.2	—	19.005 ± 0.055	19.355 ± 0.060	18.518 ± 0.054	—	—	Iowa
2018-03-26.32	203.82	71.0	20.127 ± 0.376	19.127 ± 0.238	—	18.576 ± 0.108	18.748 ± 0.092	—	LCOGT
2018-03-27.49	204.99	72.2	—	19.062 ± 0.051	19.550 ± 0.030	18.547 ± 0.039	—	—	Iowa
2018-03-28.48	205.98	73.1	—	19.163 ± 0.053	19.556 ± 0.045	18.695 ± 0.059	—	—	Iowa
2018-03-29.48	206.98	74.1	—	—	—	—	18.783 ± 0.045	—	PO
2018-04-02.48	210.98	78.0	—	19.389 ± 0.045	—	—	—	—	PO
2018-04-05.16	213.66	80.6	20.458 ± 0.088	19.534 ± 0.034	19.949 ± 0.054	19.011 ± 0.018	18.890 ± 0.034	18.707 ± 0.034	LT
2018-04-05.46	213.96	80.9	—	19.472 ± 0.098	19.829 ± 0.062	18.878 ± 0.058	—	—	Iowa
2018-04-05.48	213.98	80.9	—	—	—	18.925 ± 0.035	—	—	PO
2018-04-06.48	214.98	81.8	—	—	—	—	18.986 ± 0.052	—	PO
2018-04-08.40	216.90	83.7	—	19.593 ± 0.039	—	—	—	—	PO
2018-04-12.18	220.68	87.4	20.601 ± 0.256	19.670 ± 0.129	20.091 ± 0.100	19.167 ± 0.047	19.113 ± 0.044	18.965 ± 0.080	LT
2018-04-14.14	222.64	89.3	20.566 ± 0.048	19.734 ± 0.027	20.134 ± 0.034	19.181 ± 0.026	19.121 ± 0.030	18.890 ± 0.031	LT
2018-04-18.12	226.62	93.1	20.704 ± 0.044	19.890 ± 0.041	20.246 ± 0.037	19.327 ± 0.034	19.272 ± 0.050	19.002 ± 0.041	LT
2018-05-05.06	243.56	109.6	21.217 ± 0.130	20.368 ± 0.055	20.840 ± 0.062	19.859 ± 0.026	19.852 ± 0.036	19.520 ± 0.062	LT
2018-05-08.06	246.56	112.5	21.389 ± 0.073	20.550 ± 0.049	20.908 ± 0.044	19.981 ± 0.035	19.943 ± 0.063	19.643 ± 0.083	LT
2018-05-18.02	256.52	122.1	21.422 ± 0.070	20.799 ± 0.052	21.159 ± 0.046	20.257 ± 0.046	20.376 ± 0.045	19.849 ± 0.060	LT
2018-05-23.00	261.50	127.0	21.685 ± 0.176	20.912 ± 0.088	21.218 ± 0.085	20.428 ± 0.040	20.434 ± 0.064	20.102 ± 0.098	LT
2018-06-02.97	272.47	137.6	21.842 ± 0.084	21.223 ± 0.051	21.478 ± 0.056	20.617 ± 0.033	20.773 ± 0.050	20.398 ± 0.071	LT
2018-06-08.02	277.52	142.5	—	—	—	20.723 ± 0.037	—	—	LT
2018-06-21.07	290.57	155.2	22.137 ± 0.127	21.599 ± 0.089	21.858 ± 0.069	21.011 ± 0.060	21.211 ± 0.175	20.943 ± 0.158	LT
2018-06-24.04	293.54	158.0	—	—	—	21.111 ± 0.084	—	—	LT
2018-07-03.04	302.54	166.8	—	—	—	21.317 ± 0.102	—	—	LT
2018-07-14.96	314.46	178.3	—	22.122 ± 0.121	—	21.528 ± 0.079	—	—	LT
2018-08-17.89	348.39	211.2	23.300 ± 1.000	22.900 ± 0.500	22.700 ± 0.800	22.180 ± 0.400	22.332 ± 0.500	—	SPEC

NUV photometry.

UT Date (yyyy-mm-dd)	JD 2458000+	Phase ^a (day)	<i>uvw2</i> (mag)	<i>uvm2</i> (mag)	<i>uvw1</i> (mag)	<i>uvu</i> (mag)	Tel ^b / Inst
2018-01-21.53	140.03	9.1	15.031 ± 0.042	14.811 ± 0.042	14.870 ± 0.044	14.974 ± 0.041	UVOT
2018-01-23.86	142.36	11.4	15.112 ± 0.044	14.930 ± 0.043	14.853 ± 0.045	15.074 ± 0.044	UVOT
2018-01-24.91	143.41	12.4	15.259 ± 0.041	15.023 ± 0.042	14.938 ± 0.039	—	UVOT
2018-01-26.05	144.55	13.5	15.509 ± 0.041	15.314 ± 0.043	15.151 ± 0.040	—	UVOT

Table 1 - continued.

UT Date (yyyy-mm-dd)	JD 2458000+	Phase ^a (day)	<i>uvw</i> 2 (mag)	<i>uvm</i> 2 (mag)	<i>uvw</i> 1 (mag)	<i>uvu</i> (mag)	Tel ^b / Inst
2018-01-31.02	149.52	18.4	16.319 ± 0.053	16.025 ± 0.050	15.848 ± 0.052	15.511 ± 0.045	UVOT
2018-02-02.16	151.66	20.4	16.662 ± 0.060	16.434 ± 0.055	16.097 ± 0.057	15.729 ± 0.051	UVOT
2018-02-04.61	154.11	22.8	16.998 ± 0.085	16.831 ± 0.092	16.596 ± 0.084	15.955 ± 0.065	UVOT
2018-02-06.01	155.51	24.2	17.639 ± 0.119	17.222 ± 0.096	16.778 ± 0.074	16.139 ± 0.060	UVOT
2018-02-09.80	159.30	27.8	17.951 ± 0.130	—	17.283 ± 0.091	16.596 ± 0.068	UVOT
2018-02-12.71	162.21	30.7	18.546 ± 0.164	18.670 ± 0.180	17.873 ± 0.136	16.856 ± 0.080	UVOT
2018-02-18.04	167.54	35.8	19.175 ± 0.241	20.036 ± 0.452	18.630 ± 0.215	17.477 ± 0.109	UVOT
2018-02-23.75	173.25	41.4	20.774 ± 0.843	—	18.894 ± 0.265	18.216 ± 0.187	UVOT
2018-02-26.53	176.03	44.1	20.268 ± 0.533	20.232 ± 0.561	19.360 ± 0.370	18.716 ± 0.245	UVOT
2018-02-28.52	178.02	46.0	21.059 ± 0.735	—	—	18.689 ± 0.180	UVOT
2018-03-05.43	182.93	50.8	—	—	20.432 ± 0.696	19.254 ± 0.317	UVOT
2018-03-06.49	183.99	51.8	—	—	—	18.999 ± 0.294	UVOT

NIR photometry.

UT Date (yyyy-mm-dd)	JD 2458000+	Phase ^a (day)	<i>J</i> (mag)	<i>H</i> (mag)	<i>K</i> (mag)	Tel ^b /Inst
2018-03-12.19	189.69	57.3	17.284 ± 0.047	17.012 ± 0.100	16.706 ± 0.163	NC
2018-03-30.57	208.07	75.1	18.019 ± 0.061	17.695 ± 0.042	—	UKIRT
2018-05-16.43	254.93	120.6	19.438 ± 0.081	18.448 ± 0.056	—	UKIRT
2018-06-03.60	273.10	138.2	19.942 ± 0.138	18.915 ± 0.096	—	UKIRT
2018-06-04.28	273.78	138.9	—	18.861 ± 0.096	—	UKIRT
2018-06-28.44	297.94	162.3	20.515 ± 0.196	19.307 ± 0.112	—	UKIRT

^aRest frame days with reference to the explosion epoch JD 2,458,130.6.

^bThe abbreviations of telescope/instrument used are as follows: ASASSN - ASAS-SN quadruple 14-cm telescopes; LCOGT - Las Cumbres Observatory 1 m telescope network; LT - 2m Liverpool Telescope; DN - 0.5m DEMONEXT telescope; PO - 0.6m telescopes of Post observatory; Iowa - 0.5m Iowa Robotic Telescope; SPEC - synthetic photometry using GTC spectrum; NC - NotCAM NIR imager mounted on 2.6m NOT; UKIRT - WFCAM NIR imager mounted on 3.8m UKIRT; UVOT - *Swift* Ultraviolet Optical Telescope. Data observed within 5 hr are represented under a single-epoch observation.

Table 2. Summary of spectroscopic observations of ASASSN-18am.

UT Date	JD – 2,458,000	Phase ^a (day)	Telescope / Instrument
2018-01-14.54	133.04	2.4	FLWO/FAST
2018-01-20.27	138.77	7.9	NOT/ALFOSC
2018-01-20.66	139.16	8.3	Keck/LRIS
2018-01-22.22	140.72	9.8	NOT/ALFOSC
2018-01-24.48	142.98	12.0	Palomar/DBSP
2018-01-26.87	145.37	14.3	Xinglong/BFOSC
2018-01-30.87	149.37	18.2	Xinglong/BFOSC
2018-01-31.49	149.99	18.8	MDM/OSMOS
2018-02-01.52	151.02	19.8	MDM/OSMOS
2018-02-02.49	151.99	20.7	MDM/OSMOS
2018-02-09.54	159.04	27.6	Shane/Kast
2018-02-13.24	162.74	31.2	NOT/ALFOSC
2018-03-04.47	181.97	49.8	MDM/OSMOS
2018-03-23.26	200.76	68.0	NOT/ALFOSC
2018-04-05.15	213.65	80.6	NOT/ALFOSC
2018-05-18.35	256.85	122.5	LBT/MODS
2018-08-17.89	348.39	211.2	GTC/OSRIS

^aRest-frame days with reference to the explosion epoch JD 2,458,130.6.
See §3 for telescope and instrument details.

Table 3. X-ray detections and upper limits

UT Date (yyyy-mm-dd)	JD 2458000+	Phase ^a (day)	Flux ^b (10^{-13} ergs s ⁻¹ cm ⁻¹)	Luminosity (10^{41} erg s ⁻¹)	Tel
2018-01-20	140.03	9.1	< 1.9	< 4.5	Swift
2018-01-22	142.36	11.4	2.78 ± 1.18	6.5 ± 2.8	Swift
2018-01-23	143.41	12.4	1.82 ± 0.93	4.3 ± 2.2	Swift
2018-01-25	144.55	13.5	2.00 ± 0.92	4.7 ± 2.2	Swift
2018-01-30	149.52	18.4	< 1.8	< 4.1	Swift
2018-02-01	151.66	20.4	< 1.6	< 3.7	Swift
2018-03-14	192.19	59.7	< 0.16	< 0.38	Chandra

^a Rest frame days with reference to the explosion epoch JD 2,458,130.6.

^b Fluxes in the 0.3-10 keV band. The errors and upper-limits are 1σ values.

- ¹Department of Astronomy, The Ohio State University, 140 W. 18th Avenue, Columbus, OH 43210, USA.
- ²Center for Cosmology and AstroParticle Physics (CCAPP), The Ohio State University, 191 W. Woodruff Avenue, Columbus, OH 43210, USA.
- ³Kavli Institute for Astronomy and Astrophysics, Peking University, Yi He Yuan Road 5, Hai Dian District, Beijing 100871, China.
- ⁴Department of Physics and Astronomy, Aarhus University, Ny Munkegade 120, DK-8000 Aarhus C, Denmark
- ⁵Department of Physics, Florida State University, Tallahassee, FL 32306, USA
- ⁶INAF-Osservatorio Astronomico di Padova, Vicolo dell'Osservatorio 5, I-35122 Padova, Italy
- ⁷Harvard-Smithsonian Center for Astrophysics, 60 Garden St., Cambridge, MA 02138, USA
- ⁸Department of Astronomy, University of California, Berkeley, CA 94720-3411, USA
- ⁹Miller Senior Fellow, Miller Institute for Basic Research in Science, University of California, Berkeley, CA 94720, USA.
- ¹⁰Núcleo de Astronomía de la Facultad de Ingeniería y Ciencias, Universidad Diego Portales, Av. Ejército 441, Santiago, Chile
- ¹¹Millennium Institute of Astrophysics, Santiago, Chile.
- ¹²Tuorla Observatory, Department of Physics and Astronomy, University of Turku, FI-20014 Turku, Finland
- ¹³CAS Key Laboratory of Optical Astronomy, National Astronomical Observatories, Chinese Academy of Sciences, Beijing 100101, China
- ¹⁴School of Physics, The University of Melbourne, Parkville, VIC 3010, Australia
- ¹⁵ARC Centre of Excellence for All Sky Astrophysics in 3 Dimensions (ASTRO 3D)
- ¹⁶DARK, Niels Bohr Institute, University of Copenhagen, Lyngbyvej 2, 2100 Copenhagen, Denmark
- ¹⁷Department of Astronomy and Astrophysics, University of California, Santa Cruz, CA 95064, USA
- ¹⁸Department of Astronomy and Astrophysics, University of California, Santa Cruz, California, 95064, USA
- ¹⁹Dipartimento di Fisica e Astronomia 'G. Galilei', Università di Padova, Vicolo dell'Osservatorio 3, I-35122 Padova, Italy
- ²⁰Dept. of Physics, Earth Science, and Space System Engineering, Morehead State Univ., 235 Martindale Dr., Morehead, KY 40351, USA
- ²¹Carnegie Observatories, 813 Santa Barbara Street, Pasadena, CA 91101, USA
- ²²Department of Astronomy and The Oskar Klein Centre, AlbaNova University Center, Stockholm University, SE-10691 Stockholm, Sweden
- ²³Department of Physics and Astronomy, University of Iowa, Iowa City, IA 52242
- ²⁴Trinity University, Department of Physics & Astronomy, One Trinity Place, San Antonio, TX 78212
- ²⁵Post Observatory, Lexington, MA 02421
- ²⁶Department of Physics and Astronomy, University of California, Riverside, CA 92507, USA
- ²⁷Institute for Astronomy, University of Hawaii, 2680 Woodlawn Drive, Honolulu, HI 96822, USA